GCA-D-18-00092.R2

Incipient Chemical Weathering at Bedrock Fracture Interfaces in a Tropical Critical Zone, Puerto Rico

Oliver W. Moore[a,1*], Heather L. Buss[a], Anthony Dosseto[b]

[a] School of Earth Sciences, University of Bristol, Wills Memorial Building, Bristol BS8 1RJ, UK

[b] Wollongong Isotope Geochronology Laboratory, School or Earth and Environmental Sciences, University of Wollongong, Wollongong, NSW 2522, Australia

* Corresponding author: o.moore@leeds.ac.uk

Tel: +44(0)113 34 34696

Keywords: Luquillo Experimental Forest, critical zone, U-series nuclides, weathering rates, weathering rinds

[1] Present address: School of Earth and Environment, University of Leeds, Leeds, LS2 9JT, UK

Abstract

The processes that control chemical weathering of bedrock in the deep critical zone at a mm-scale are still poorly understood, but may produce 100s of meters of regolith and substantial fluxes of silicate weathering products and thus may be important for modeling long-term, global CO_2. Weathering controls are also difficult to ascertain, as laboratory determined dissolution rates tend to be 2-5 orders of magnitude faster than field determined dissolution rates. This study aims to establish (i) the incipient processes that control the chemical weathering of the Bisley bedrock and (ii) why weathering rates calculated for the watershed may differ from laboratory rates (iii) why rates may differ across different scales of measurement. We analyzed mineralogy, elemental chemistry, and porosity in thin sections of rock obtained from drilled boreholes using Scanning Electron Microscopy (SEM) with energy dispersive spectrometry, electron probe microanalysis, and synchrotron-based Micro X-ray Fluorescence (μXRF) and X-ray Absorption Near Edge Structure (XANES). Weathering ages were determined from U-series isotope analysis. Mineral specific dissolution rates were calculated from solid-state mineralogical gradients and weathering ages. Mineralogical and elemental transects across thin sections and SEM images indicate that trace pyrite is the first mineral to dissolve. Micro-XRF mapping at 2 μm resolution revealed sulfate in pore space adjacent to dissolving pyrite, indicating that the incipient reaction is oxidative. The oxidative dissolution of pyrite produces a low pH microenvironment that aids the dissolution of pyroxene and chlorite. The rate-limiting step of weathering advance, and therefore the creation of the critical zone in the Bisley watershed, is pyrite oxidation, despite the low abundance (~0.5 vol %) of pyrite in the parent rock. The naturally determined dissolution rates presented here either approach, converge with, or in some cases exceed, rates from the literature that have been experimentally determined. The U-series weathering age data on the mm-scale integrates the weathering advance rate over the ~4.2 ± 0.3 kyrs that the weathering rind took to form. The weathering advance rate calculated at a watershed scale (from stream chemistry data) represents a contemporary weathering advance rate, which compares well with that calculated for the weathering rind, suggesting that the Bisley watershed has been weathering at steady-state for the last ~4 kyrs.

1. INTRODUCTION

Identifying and quantifying deep Critical Zone (CZ) weathering mechanisms is crucial to understanding the landscape evolution of the Earth's surface and the development and regulation of the CZ as a whole (Buss et al., 2008; 2013; Dosseto et al., 2012; Graham et al., 2010; Holbrook et al., 2014; Rempe and Dietrich, 2014; Riebe et al., 2017; St. Clair et al., 2015). In humid tropical catchments with very high weathering rates, weathering along deep CZ rock fractures likely controls the solute weathering flux to the hydrosphere (Chapela Lara et al., 2017; Kurtz et al., 2011; Schopka and Derry, 2012; White et al., 1998) and the flux of nutrients to the subsurface biosphere (Buss et al., 2005; 2008; 2010). Chemical weathering is one of the primary rate-limiting steps of the global geochemical cycle as a whole (Barth, 1961). In this regard, chemical weathering also exerts a major control on the global carbon cycle, regulating atmospheric CO_2 over geologic timescales (Berner et al., 1983; Walker et al., 1981). Therefore, controls on deep chemical weathering processes may be critical in terms of understanding and modeling global climate. However, the relative importance of chemical weathering in the deep CZ versus that in soils, and the processes that control deep weathering rates (whole-rock and mineral-specific), are still poorly understood (Anderson and Dietrich, 2001; Buss et al., 2005; 2008; 2010; Tipper et al., 2006).

Hot-spots of chemical weathering may dominate global silicate weathering fluxes. In particular, the tropical regions supply the majority of the dissolved Si that reaches the world's oceans, despite covering only a quarter of the land mass (Meybeck, 1987; Stallard and Edmond, 1983) and report some of the highest weathering rates in the world (e.g., Buss et al., 2008; Dosseto et al., 2012; Schulz and White, 1999; White and Blum, 1995). Similarly, volcanic islands are weathering hotspots, where dissolution of Ca and Mg bearing silicate rocks leads to an estimated sequestration of 30-35% of global CO_2 (Dessert et al., 2003). On volcanic islands, deep CZ weathering rates are 2 to 5 times higher than surface weathering rates (Rad et al., 2007), resulting in ~15 times more CO_2 (of the sequestered 30-35%) being consumed via groundwater flow along subsurface bedrock fractures, versus that consumed by surface waters reacting with regolith (Schopka and Derry, 2012). Throughout this study, regolith is defined as all material overlying or surrounding intact bedrock, including the saprolite (an isovolumetric weathering product that retains the structure of the original parent material) and the soil (the portion of the weathering profile that no longer retains any of the parent structure).

Some previous attempts to quantify weathering rates in the field have extrapolated surface processes to the deep (e.g., McKean et al., 1993; Pavich et al., 1985), or averaged elemental loss over the entire regolith profile or watershed (e.g., Gaillardet et al., 2011; Schulz and White, 1999; Von Blanckenburg, 2005; White et al., 2001). These methods generally require the assumption of a steady-state weathering profile, whereby the weathering advance rate (WAR) through the bedrock must equal the surface erosion rate i.e., the profile thickness is constant (Fletcher et al., 2006; White, 2002). Several studies have proposed mechanisms by which processes at the atmosphere-regolith interface are coupled with those at the regolith-bedrock interface, for example, via O_2 infiltration (Fletcher et al., 2006), temperature, runoff, erosion (West et al., 2005) and precipitation (Riebe et al., 2004). However, very few studies have tested the steady-state assumption (Riebe et al., 2004), for example, by comparing surface erosion rates determined from cosmogenic isotope abundances to regolith production rates calculated from U-Th disequilibria (e.g., Carretier et al., 2014; Dellinger et al., 2015; Dosseto et al., 2008; 2012). The work presented here aims to address this knowledge gap by comparing weathering rates calculated over different spatial and temporal scales, as well as depths, to test the steady-state assumption.

Extrapolation of surface observations to the deep critical zone assumes that the same processes, with the same controls, function in both zones. Within much of the humid tropics, the surface ecosystem is separated from deep ecosystems by thick regolith (10s-100s of meters deep), depleted in base cations and mineral nutrients and characterized by a sharp weathering front, producing nutrients close to the bedrock-regolith interface (e.g., Buss et al., 2010; 2017). As a result, the surface ecosystem is reliant upon the shallow recycling of nutrients (Herrera et al., 1978a; 1978b; McDowell, 1998; 2001; Stark and Jordan, 1978; White et al., 1998) with atmospheric inputs an integral source of nutrients (e.g., McTainsh, 1980; Pett-Ridge, 2009; Stoorvogel et al., 1997). Also, in some regolith profiles, O_2 concentrations decrease with depth as CO_2 increases substantially (Brantley et al., 2014; Buss et al., 2017; Liptzin et al., 2011; Richter and Markewitz, 1995). This partitioning makes it probable that the weathering mechanisms at the bedrock-regolith interface are fundamentally different from those at the surface.

If the weathering mechanisms at the surface are decoupled from those at depth, both zones must be examined individually at a spatial scale consistent with the extent of the reactions. For example, in the Río Icacos watershed of Puerto Rico, petrographic, mineralogical and

elemental analysis across a granitic bedrock-regolith transition of about 50 cm, revealed that complete depletion of plagioclase, chlorite and apatite occurs over the entire transition and complete hornblende depletion only occurs over the outer 7 cm (Buss et al., 2008; 2010; Turner et al., 2003). In contrast, within the same weathering profile, biotite depletion begins in the transition zone (Buss et al., 2008), but continues throughout the overlying 4-6 m of saprolite (Murphy et al., 1998) and quartz dissolves (partially) over most of the saprolite profile (2.4 – 8.5 m) (Schulz and White, 1999). If solid-state dissolution rates of these minerals were integrated over the entire regolith or watershed without an upscaling treatment, the rates would be underestimated as they are likely slower in the regolith than at the rock-regolith interface where minerals are fresher. Underestimation of rates may then lead to misinterpretation of their influence on spatially discrete CZ processes (e.g., vegetation growth, subsurface microbial cycles and groundwater evolution). Furthermore, underestimation by inappropriate averaging of weathering data over entire regolith profiles or watersheds may contribute to the so-called field-laboratory discrepancy of 2-5 orders of magnitude between lab calculated and field calculated mineral dissolution rates (e.g., White and Brantley, 2003), further highlighting the need for greater knowledge of deep CZ weathering rates..

Quantification of natural weathering rates, in the context of other CZ processes is essential to modeling the evolution of the continental surface. To establish and model the controls on whole-rock weathering rates, mineral-specific weathering rates, and weathering export rates, and therefore the response of the CZ to current and future environmental drivers, the identification of the weathering mechanisms and rate-limiting steps are also crucial. Extrapolating from chemical kinetics, the rate-limiting step can be conceptualized as the 'bottleneck' in the 'supply chain' of nutrients and soil from the bedrock to the rest of the CZ, limiting its overall productivity (Field et al., 2015). For instance, regardless of whether a mineral present in the rock has a fast kinetic dissolution rate or not, if the reactive fluid is highly saturated with regard to a weathering product (i.e., at thermodynamic equilibrium), or undersaturated with a reactant (e.g., CO_2), then the mineral dissolution will proceed more slowly than the kinetic rate. For example, in the Landscape Evolution Observatory, Arizona, USA, van Haren et al. (2017) found that reduced CO_2 diffusion into pore space limited basalt weathering rates, shifting the balance towards equilibrium.

Chemical weathering of rocks commonly begins with grain-scale infiltration of meteoric water, which is largely controlled by the texture of the parent material (e.g., grain size distribution, permeability, porosity) (Bazilevskaya et al., 2013). Mineral dissolution rates tend to be slow at this initial stage, as they depend on the rate of diffusion into (and out of) the solid rock (transport limited). Subsequent micro- or macro-fracturing or other types of porosity development allows advective infiltration of reactive fluids into the rock and greater access to fresh minerals, enabling chemical weathering to proceed more rapidly (Buss et al., 2008; Navarre-Sitchler et al., 2011; Mironenko and Cherkasova, 2017). As porosity develops, the advance of the weathering front may cease to be transport-limited, and instead become kinetics-limited (Navarre-Sitchler et al., 2011).

Regardless of the incipient process by which water infiltrates fresh parent rock and initiates chemical weathering, if water-rock interactions persist and if the chemical WAR (weathering advance rate) is greater than the physical erosion rate, a rind may form. Weathering rinds are residual outer layers of chemical alteration. They are generally formed isovolumetrically and are composed of secondary minerals (e.g., metal oxides and clays) and weathering-resistant primary minerals (e.g., quartz) (Buss et al., 2013; Navarre-Sitchler et al., 2011; Pelt et al., 2008; Sak et al., 2004; 2010). Often visible to the naked eye, rinds are commonly denoted by discoloration and increased porosity, relative to the un-weathered parts of the rock. Once a rind has developed, grain-scale infiltration of meteoric water to the fresh rock is then controlled by the permeability and diffusivity of the rind's pore network (Navarre-Sitchler et al., 2009). Assuming that rind thickness is directly related to the time over which weathering has occurred, mineralogical and elemental gradients across weathering rinds can be used not only to identify weathering mechanisms, but also to determine relative rates of mineral-specific reactions over the timescale of rind development.

Due to issues of accessibility (e.g., vegetation cover, thick regolith and conservation restrictions), few studies are conducted to determine the weathering mechanisms, whole-rock and mineral-specific weathering rates and the rate-limiting step along deep bedrock fractures, where the majority of weathering occurs in the tropics (Hynek et al., 2017). Here we document in-situ weathering processes that occur in a deep, tropical CZ, located in the Luquillo Experimental Forest on Puerto Rico, an island of volcanic origin. We used U-Th isotopic disequilibria across weathering rinds to determine whole-rock weathering rates and to provide a time constraint to calculate mineral-specific dissolution rates over the mm-scale

weathering hot-spot (Buss et al., 2013; 2017). This method affords a mechanistic understanding of the initial formation of the CZ based directly on observations of deep CZ weathering reaction fronts. We also compared our rates to laboratory-determined mineral dissolution rates from the literature and to whole-rock weathering rates measured on different spatial and temporal scales to identify and understand the scale-dependence of our rates.

2. METHODS

2.1 Field site

The Bisley 1 watershed is one of five neighboring catchments within the Luquillo Experimental Forest in NE Puerto Rico and is a key study site of the Luquillo Critical Zone Observatory (LCZO) (Fig. 1). These catchments feed into the Mameyes River, which discharges into the Atlantic Ocean. The 30+ m thick regolith (Buss et al., 2013) is interspersed with bedrock corestones of the Fajardo formation, a marine bedded meta-volcaniclastic rock that was initially deposited in a near sea-surface complex ~100 Ma (Briggs and Aguilar-Cortés, 1980; Jolly et al., 1998). The area then underwent low-grade contact metamorphism, including hydrothermal alteration, as a result of the subsequent intrusion of the nearby Río Blanco quartz diorite stock ~60 Ma (Smith et al., 1998).

The Bisley watershed's topography is characterized by steep slopes that vary in elevation from 260 to 400 masl over a 6.7 km^2 area (Scatena, 1989). The climate is humid and subtropical, with precipitation in every month. Mean annual temperatures decrease with elevation, from around 23.5-27 ^oC in the lower elevations to 17-20 ^oC in the upper reaches (Schellekens et al., 2004). Rainfall in the Luquillo Mountains increases with altitude from about 2500 to 4500 mm yr^{-1} over 1200 m of elevation (Garcia-Martino et al., 1996), with the Bisley watersheds experiencing an average rainfall of 3482 mm yr^{-1} between 1988 and 2003 (Heartsill-Scalley et al., 2007). Of this rainfall, approximately 28% falls in less than 10% of calendar days (Scatena, 1989), resulting in a rapid streamflow response that is dominated by fast, near-surface flow paths (Schellekens et al., 2004). Despite the evident near-surface flow paths, deeper infiltration must occur, as the Bisley 1 stream flows year round. The deeper flow paths likely run through the bedrock which has regularly distributed fractures (Hynek et al., 2017). Indeed, Mg isotope signatures in the Bisley 1 stream water at base flow have been

interpreted to reflect substantial chlorite dissolution (Chapela Lara et al., 2017), which only occurs at rock-regolith interfaces, deep in the Bisley CZ (Buss et al., 2017).

2.2 Field sampling and sample preparation

In 2010 a wireline drilling campaign was conducted on Road 915, near the stream gage for the Bisley 1 catchment and along the spine of the local ridge that borders the catchment (Buss et al., 2013). Samples in this work originate from borehole, B1W1 (N18 18.933 W65 44.748, referenced to NAD83 datum; see Fig. 1) drilled to 37.2 m depth (Buss et al., 2013). Drilling was conducted by Geo Cim Inc. (Guaynabo, Puerto Rico), using a hydraulic rotary drill with diamond-impregnated drill bits. Bisley 1 stream water was used as the only drilling fluid. The weathering advance rate of the Bisley 1 regolith has also been previously investigated at location B1R (Fig. 1) by Dosseto et al. (2012).

Extensive optical petrographic microscopy and preliminary SEM of thin sections from throughout this borehole and another borehole noted abundant weathered fracture surfaces in the recovered rock, with visible rinds up to 15 mm thick (Buss et al., 2013). Most of these rinds were 3-10 mm thick. For the present study, we selected two adjacent samples, B1W1-1-4 and B1W1-1-5 (from a depth of 3.4 m), which we deemed representative as they have approximately 6 mm thick weathering rinds and unweathered mineral and elemental compositions (i.e., at the region of the thin sections furthest from the rinds) close to the mean for the bedrock (average of 18 samples; Buss et al., 2013). These two samples are analogues, as they are from the opposing sides of a fracture, meaning they have undergone the same degree of weathering for the same period of time and both display the same thickness of rind. B1W1-1-5 was used for elemental and mineralogical analysis and cut perpendicular to the fracture surface (Fig. S1). Following vacuum impregnation with Epo-Tek 301 epoxy resin, multiple 30 µm thick petrographic thin sections were then made with dimensions of 27 x 46 mm (Spectrum Petrographics, Inc., Vancouver, WA) to cover the entire weathering profile of the sample. Thin sections were then finished with a 0.5 µm diamond polish. To minimize the interaction of samples with water, the material was only exposed to an anhydrous cooling/lubricant fluid throughout the preparation process. Sample B1W1-1-4 was reserved for U-Th analysis and inductively coupled plasma – optical emission spectrometry (ICP-OES) (Fig. S2).

246

247 **2.3 Microscopic analysis**

248 To determine the spatially resolved, elemental composition of the weathering rocks (which
249 can then be used to determine the mineralogical composition), a Hitachi S-3500N scanning
250 electron microscope (SEM) was used in conjunction with a Thermo Scientific 10 mm^2
251 Silicon Drift Detector (SDD) (35^o take off angle) to couple backscattered electron (BSE)
252 imaging with micrometer scale X-ray elemental maps traversing from the unweathered parent
253 material up to the edge of the weathered fracture surface (Fig. S1B). The SEM was operated
254 at an accelerating potential of 20 kV for all X-ray elemental maps. The elemental maps were
255 produced by rastering the electron beam automatically with the SDD recording the number of
256 X-ray counts at different excitation energies (which correspond to different elements).
257 Elemental X-ray maps were produced with a 1024 x 1024 pixel resolution with 40 frames per
258 map and a frame time of 100 s, resulting in an average dwell time of 95 µs. To determine
259 mineral modal abundances, phase analysis was conducted on the elemental X-ray maps using
260 the Noran System Seven (NSS) V3.2 software. Briefly, pixels with similar X-ray spectra are
261 grouped together and attributed by the user to a specific mineral, based on the elemental
262 composition and crystal morphology. Porosity was determined from the areas of X-ray maps
263 that have an elemental composition of SiO_2 (the glass of the thin section) and identified by
264 the user as visually distinct from quartz (pore space appears black and quartz as grey on BSE
265 images). To calculate the mean area percentages of each mineral, five X-ray phase analysis
266 maps from the furthest area inboard of the fracture surface, measuring 2.8 mm by 2.1 mm
267 were averaged. Then the two-dimensional area percentages were projected into the third-
268 dimension to produce volume percentages of minerals, assuming a homogenous distribution
269 and that the dimensions of the mineral grains are the same in the z dimension as in the xy,
270 with the uncertainty presented as 1SE. To obtain statistically significant counts and a good
271 signal/noise ratio for the X-ray mapping, an accelerating voltage of 20 kV was necessary. X-
272 ray phase analysis was used in favor of XRD due to the higher sensitivity and spatial
273 resolution of the method, previously XRD analysis of the Bisley bedrock failed to detect the
274 presence of pyrite which was detected by SEM (Buss et al., 2013).

275 To determine profiles of elemental and mineralogical changes across the rock weathering
276 fronts, five X-ray map transects were produced parallel to the propagation of the weathering

front, running from the fracture surface into the parent rock (Fig. S1) and averaged. The uncertainty is presented as one standard error of the mean (1SE) of the five transects and propagated through all calculations using standard error propagation rules.

To corroborate the results of the elemental X-ray maps, bulk solid-state elemental concentrations were also analyzed by ICP-OES following lithium metaborate fusion, on samples drilled along a ~50 mm transect in sample B1W1-1-4 using a handheld rotary tool with a diamond impregnated bit (Fig. S2). The uncertainty of the ICP-OES data is presented as 1SE of a local rock standard analyzed repeatedly over several years, or where larger, the detection limit of the method.

Element oxide compositions of minerals were determined quantitatively on a five-spectrometer Cameca SX100 electron microprobe at the University of Bristol, run at 20 KeV using a 10 nA regulated beam current, with a focused beam. To measure K, Ca, Cr and Ti, LPET crystals were used; TAP crystals for Na, Mg, Si and Al and an LLIF crystal for Fe and Mn. The set up was then calibrated against a range of mineral, oxide and metal standards. Counting times for most elements were 30 s on peak and 15 s on the background. Na was measured first to prevent migration, however, due to the high concentrations of Na no mobility was observed. A diopside standard and amphibole standard were run in triplicate as unknowns at the beginning of each analytical session.

Mineral diameters were measured from BSE images using the ImageJ image processing software (National Institute of Mental Health, Maryland). The sample size was 50 for each mineral and the diameter is presented as the mean of this population with the uncertainty presented as 1SE. An SEM image's scale bar was measured 100 times, to determine an accuracy of -0.06 % between the measured and actual length, with a precision of 3% from the average measured length.

2.4 Weathering alteration analyses

2.4.1 CIA

The chemical index of alteration (CIA) of silicate rocks was calculated to document the loss of mobile base cations Ca, Na and K, relative to Al, which is assumed to be relatively immobile (Nesbitt and Young, 1982):

$$CIA = \frac{Al_2O_3}{(Al_2O_3+CaO+Na_2O+K_2O)} \times 100 \quad (1)$$

The CaO included in the CIA calculation includes only that which is incorporated in silicate minerals and excludes the fraction present in carbonates or phosphates, if present (Bahlburg and Dobrzinski, 2011; Fedo et al., 1995). However, as the CIA relates the losses to Al_2O_3, it actually documents the degree of weathering of *alumino*silicate minerals, with particular note to feldspars weathering to clay minerals. Values of CIA for parent material are typically ≤55 and increase with the degree of weathering to a maximum of 100 (Nesbitt and Young, 1982). The CIA therefore gives a rough indication as to what depth in the profile can be deemed as unweathered parent material for other analyses such as U-series and the mass transfer coefficient (as described below), where a parent sample is required.

2.4.2 Mass transfer coefficient

Chemical weathering produces profiles that record (i) the loss of mobile components (elemental or mineralogical) from a parent rock, (ii) the addition of components from external sources and (iii) the translocation of elements within a profile. By definition, the total mass of an immobile component in a weathering profile remains the same in the weathered material as in the parent material. However, when mobile components are lost from the system, lowering the density of the material, the solid-state concentration (or mass fraction) of the immobile component increases. Therefore, by normalizing the measured solid-state concentrations of mobile components (elements or minerals) to an immobile component, the net mass loss or gain of the mobile component, relative to the parent material can be determined (Anderson et al., 2002; Brimhall and Dietrich, 1987):

$$\tau_{i,j} = \left(\frac{C_{j,w}C_{i,p}}{C_{j,p}C_{i,w}}\right) - 1 \quad (2)$$

where τ = mass transfer coefficient, i = immobile component, j = component of interest, C = mass fraction (wt %), p = parent material and w = weathered material. When $\tau_{i,j} = 0$, no mobilization of j has occurred relative to the parent composition. When $\tau_{i,j} = -1$, component j is completely depleted and when $\tau_{i,j} > 0$, component j has been gained relative to the parent composition. Therefore, τ can be used to track the progress of weathering through a profile.

To establish the least mobile component for the calculation of τ, the immobility of components were tested using volumetric strain. Isovolumetric weathering involves the removal and/or addition of components to the weathering profile with neither compaction nor dilation (Gardner, 1980). As weathering rinds are isovolumetric weathering products, it follows that the change in volume resulting from volumetric strain should be near zero for an immobile element (Ague, 1994; Brimhall and Dietrich, 1987), calculated by:

$$\varepsilon_{i,w} = \frac{\rho_p C_{i,p}}{\rho_w C_{i,w}} - 1 \quad (3)$$

where $\varepsilon_{i,w}$ = the volumetric strain (Fig. S4) in the weathered (w) sample with respect to a putative immobile component (i), ρ_w = the bulk density of the weathered material (g cm^{-3}), ρ_p = the bulk density of the parent (p) material (g cm^{-3}), $C_{i,w}$ = the mass fraction of component *i* in the weathered sample (g g^{-1}) and $C_{i,p}$ = the mass fraction of component *i* in the parent material (g g^{-1}).

We quantified mass transfer (τ) across the Bisley weathering rind profiles using Eq. 2, which is applicable when the parent material is homogeneous and an immobile element is present in both the parent and weathered materials. The Fajardo formation bedrock is of homogenous age (Albian) and possesses several relatively immobile elements that are readily measured using X-ray elemental analysis (Ti, Al, Si) in the parent and weathered material as determined above. Other immobile elements such as Zr are present in rock but in very low concentrations and heterogeneously distributed, meaning that the uncertainty associated with them is too great to make meaningful interpretations when propagated through calculations. The composition of the rock ranges between andesite and basaltic andesite and the grain size varies (Buss et al., 2013); geochemical and textural heterogeneity were accounted for by averaging multiple transects along the thin sections from the parent material, through the rind to the fracture surface, perpendicular to the weathering front (Fig. S1).

2.4.3 Mineral specific dissolution rates

White (2002) showed that a solid-state depletion profile for a given weathering component within regolith can be used to calculate a rate of loss for the component as a function of the WAR (also referred to as the weathering velocity, Fig. S3). However, to calculate mineral-specific dissolution rates, τ cannot be used as it is dimensionless. Therefore, we convert τ to an equivalent parameter, C_w (mol kg^{-1}):

$$C_w = C_{j,p}(\tau_{i,j} + 1) \quad (4)$$

where $C_{j,p}$ is the mass fraction of element j in the parent material. Assuming 1-D vertical transport, a decrease (Fig. S3) in the normalized concentration of a mineral or element from the initial mass fraction (e.g., g mineral g^{-1} rock) C_0, at depth Z_0, to a weathered state (C_w) at depth Z_1, represents a loss of that component from the parent material (White, 2002). In the case of an element, this loss is only represented if it is not incorporated into a secondary mineral. In a soil or regolith profile formed on homogeneous parent material, the C_w of a weathering, mobile component generally decreases with distance from the parent material, describing a weathering reaction front in reference to the bedrock-regolith interface. In a weathering rind profile, weathering reaction fronts are defined relative to the fracture surface, tracking loss of mobile components from the un-weathered interior of the rock towards the fracture. In either case, the thickness of the weathering reaction front is inversely proportional to the reaction time, such that sample points furthest from the un-weathered parent represent the longest reaction times.

If the weathering profile thickness is in steady-state (i.e., constant with time) or quasi-steady-state (where the thermodynamics of the system change slowly enough that equilibrium is maintained (Lichtner, 1988) and therefore conditions such as the WAR are constant over the timescale of profile development, mineral-specific dissolution rates can be estimated from an approximated linear gradient of the mineral's weathering reaction front and the WAR (Fig. S3; White, 2002):

$$r_m = 10^{-3} \frac{1}{\varphi S} \left(\frac{WAR}{b_s}\right) \quad (5)$$

where r_m (mol m^{-2} s^{-1}) is the mineral-specific, surface-normalized dissolution rate; φ = mass fraction of the mineral in the weathering material (g g^{-1}); S = specific surface area of the mineral (m^2 g^{-1}); WAR = solid-state weathering advance rate (m s^{-1}); b_s= slope of solid-state weathering gradient (m kg mol^{-1}) representing C_w with depth (Eq. 4, Fig. S3) and 10^{-3} is a unit conversion factor.

Some weathering rind rate models incorporate a parameter to describe diffusive transport (e.g., Navarre-Sitchler et al., 2011; Sak et al., 2004), which is used to derive a time constraint by relating diffusion coefficients to the thickness of the rind. In the present study, U-series

isotope measurements were used to more directly determine a time constraint (WAR) for Equation 5. The weathering gradient (b_s) simply describes measured mass changes across a weathering profile, and therefore Equation 5 can be used to estimate mineral-specific weathering rates in diffusive or advective weathering regimes.

In a steady-state weathering profile, a gradient in the mass transfer of a mineral (τ or C_w, Eqs. 2 and 4) with depth indicates where in the profile a reaction is occurring, that is, it defines a mineral weathering front and is inversely proportional to the rate (Eq. 5; Fig. S3). Locating the zone of reaction enables interpretation of rates in the context of other spatially variable parameters, such as porosity and pO_2. We calculated mineral-specific weathering rates (Eq. 5) using gradients determined from changes in mineral volume across the Bisley weathering rinds; these gradients track congruent mineral dissolution or transformation into a secondary mineral (e.g., kaolinite), but do not track incongruent dissolution.

2.4.4 Geometric surface area

Previous workers (Gautier et al., 2001; Mellott et al., 2002; White et al., 1996) have suggested that geometric rather than BET surface areas are more representative of reactive surface areas in the weathering environment. Therefore, to calculate the mineral specific surface area for Eq. 5, a geometric approach was used (Helgeson et al., 1984; White and Brantley, 2003), based on the average mineral grain diameter, density, geometry and roughness:

$$S = \frac{6\Lambda}{\rho_m D} \quad (6)$$

where, S = specific surface area of the mineral ($m^2\ g^{-1}$); Λ = roughness factor ($m^2\ m^{-2}$) (found to be 7 for a wide range of silicate mineral sizes (White and Peterson, 1990)); ρ_m = mineral density ($g\ cm^{-3}$) and D = average mineral grain size diameter (μm).

2.5 U-Th disequilibria

The uranium-thorium (U-Th) decay series can be used to directly measure the length of time since the introduction of water into a rock sample (e.g., Chabaux et al., 2003; 2013; Dequincey et al., 1999; 2002; Dosseto et al., 2008; 2012; Hansen and Stout, 1968; Ma et al., 2010; 2012; 2013; Pelt et al., 2008; Rosholt et al., 1966). The parent nuclide ^{238}U decays with

a half-life ($T_{1/2}$) of ~4.5 Ga to ^{234}U ($T_{1/2}$ = 244 kyr) which subsequently decays to ^{230}Th ($T_{1/2}$= 75 kyr). The half-lives of the two daughter radionuclides are on comparable timescales to Earth surface processes such as chemical weathering. If a system remains undisturbed for 5 decay half-lives of ^{234}U (roughly >1.3 Myr) then the U-series system is said to be in secular equilibrium (i.e., the flux from the daughter nuclide is equal to the flux of the parent to the daughter). When secular equilibrium is achieved, the daughter/parent activities (number of atoms of an isotope multiplied by its decay constant) are equal.

The order of mobility of the nuclides is generally viewed as $^{234}U>^{238}U>Th$ (Chabaux et al., 2003; 2008; Dosseto et al., 2008; 2012; Ma et al., 2013). Thus, a U-series disequilibrium (deviation from secular equilibrium) is established when U-bearing phases are exposed to reactive fluids (e.g., groundwater). Disequilibria in weathered material tends to show ($^{234}U/^{238}U$) < 1 and ($^{230}Th/^{238}U$) > 1 (parentheses indicate activity ratios, hereafter). The extent of disequilibria therefore records the time passed since the mineral-water interfacial area was great enough to mobilize U.

To determine U-Th isotope ratios across the Bisley weathering rinds, a transect of ten points was drilled on sample B1W1-1-4, extending 48 mm from the un-weathered interior of the rock (representing parent material) to the fracture surface (Fig. S2). A sample at each point was extracted by drilling with a 3-mm diameter carbide-tipped drill bit until a mass of ~100 mg was obtained. Each sample was then homogenized and crushed using an agate mortar and pestle. Samples were then spiked with ~30 mg of a ^{236}U-^{229}Th enriched solution and dissolved in a mixture of $HClO_4$, HF and HNO_3. Once dissolved, samples were heated to 100^{o}C to evaporate fluorides and were then dried down by step evaporation at 150^{o}C, 170^{o}C and 200^{o}C. Samples were redissolved in 1.5 M HNO_3 and loaded onto columns containing Eichrom^{TM} TRU resin to separate U and Th (Luo et al., 1997). The U and Th isotope ratios were measured on a Thermo Neptune Plus multi-collector ICP-MS at the Wollongong Isotope Geochronology Lab, University of Wollongong, following the method described in Sims et al. (2008). The precision and accuracy of the activity ratios were determined by analyzing the gravimetric standard, Quartz Latite (QLO-1) returning values of 1.006 ±0.001 (2SE) and 1.005 ±0.004 (2SE) for ($^{234}U/^{238}U$) and ($^{230}Th/^{238}U$), respectively.

2.6 U-Th Modeling

453 The calculation of the weathering advance rate of the rinds (WAR_{rind}) assumes that U-series
454 isotope fractionation within the system is controlled by weathering processes (Chabaux et al.,
455 2008; 2011; 2013; Dequincey et al., 2002; Dosseto et al., 2008; Ma et al., 2010; Pelt et al.,
456 2008). The fractionation (i.e., deviation from secular equilibrium) results from the
457 mobilization of radionuclides, which can be expressed in terms of loss and/or gain to the
458 system. Loss processes include mineral dissolution and nuclide desorption from secondary
459 minerals. Nuclides can be added to the system via illuviation processes plus sorption and co-
460 precipitation of nuclides to minerals such as Fe(III)-(hydr)oxides or clays. Aeolian deposition
461 can be another source of nuclides; however, this is generally irrelevant to weathering rind
462 studies. Assuming net losses and gains are constant with time and the weathering advance is
463 unidirectional, the temporal evolution of the number of these nuclides per gram of sample can
464 be described by Eq. 7 to 9 (Chabaux et al., 2013; Dequincey et al., 2002; Dosseto et al., 2008;
465 Ma et al., 2012). All of these equations use first order kinetic rate laws (dependent on the
466 concentration of one reactant) to describe continuous nuclide loss or gain (open system
467 conditions) and zero order rate laws (independent of the concentration of the reactants) to
468 describe nuclide gain.

469
$$\frac{\mathrm{d}^{238}U}{\mathrm{d}t} = f_{238}\,{}^{238}U_0 - k_{238}\,{}^{238}U - \lambda_{238}\,{}^{238}U \tag{7}$$

470

471
$$\frac{\mathrm{d}^{234}U}{\mathrm{d}t} = f_{234}\,{}^{234}U_0 - k_{234}\,{}^{234}U - \lambda_{234}\,{}^{234}U - \lambda_{238}\,{}^{238}U \tag{8}$$

472

473
$$\frac{\mathrm{d}^{230}Th}{\mathrm{d}t} = f_{230}\,{}^{230}Th_0 - k_{230}\,{}^{230}Th - \lambda_{230}\,{}^{230}Th + \lambda_{234}\,{}^{234}U \tag{9}$$

474 where: λ_j = decay constant (yr^{-1}) of nuclides j (here ^{238}U, ^{234}U and ^{230}Th); k_j = first order
475 nuclide loss constant (yr^{-1}) for leaching of nuclides j; and f_j = nuclide constant (yr^{-1}) of
476 nuclides j gained by the regolith. Input fluxes are presented as a proportion of the number of
477 atoms of nuclides added per year to the assumed initial quantity (expressed as $f_j N_0$).

478 By solving Eq. 7 to 9, the theoretical activities of the different nuclides in the sample at time
479 t were determined. These activities were then used to calculate the two independent activity

ratios ($^{234}U/^{238}U$) and ($^{230}Th/^{238}U$). The nuclide activities and the activity ratios are expressed as a function of the mobility parameters (k_j, f_j), the initial activities of the different nuclides and time (t) (Chabaux et al., 2013). For these calculations, t is the time elapsed between the initial reference state (t = 0) and the current stage of weathering. If the reference state sample has not undergone sufficient weathering (where mineral-water interactions are great enough that U series isotopic fractionation occurs), then t represents the weathering age of the rock. The reference state, t = 0, was taken as the furthest sample inboard of the weathering front, with a distance of z from the sample being considered. Even if the sample used as the reference state has undergone weathering it can still be used to determine the WAR_{rind}, as t (kyr) will be the interval of time passed since the considered sample was at the same relative position to the weathering front as the reference state, giving depth, z (mm); WAR_{rind} i.e., velocity (mm kyr^{-1}) was then calculated by Eq. 10.

$$WAR_{rind} = z/dt \quad (10)$$

If all mobility parameters are constrained, and nuclide fractionation only occurs at the weathering front, then the analysis of just two points (the reference state and a point that has undergone weathering) are required to calculate dt and thus WAR_{rind}. Although this is theoretically sound, in practice, parent rock samples are not always at secular equilibrium and the mobility parameters are not usually defined.

For simplicity, nuclide loss and gain were assumed to be constant across the sample (from the unweathered parent rock into the rind) (Dequincey et al., 2002; Ghaleb et al., 1990; Ma et al., 2012). The assumption of constant loss and gain is valid because the processes governing the loss and gain of nuclides is likely to be the same across the mm-scale of the study. The measured disequilibria in the samples were then used to determine the mobility parameters and the age of the individual samples relative to the parent sample (Chabaux et al., 2013). WAR_{rind} was then calculated from the variation of weathering age of individual samples as a function of distance (z) from the parent sample, assuming the WAR_{rind} is constant over z. As Th may be mobile (Ma et al., 2010; Dosseto et al., 2014), this system had 7 unknowns: six mobility parameters (a loss and gain parameter for each isotope) to be determined plus one weathering age (t) for each sample. Assuming that WAR_{rind} and the aforementioned mobility parameters are constant with time, ($^{234}U/^{238}U$) and ($^{230}Th/^{238}U$) ratios were needed for a minimum of four samples from different depths in the weathering profile to calculate Eq. 7-9.

Using the U-Th isotope ratios measured on the 10 samples from our 48 mm transect, these equations yielded the individual change in time (dt) since each sample at distance z from the reference sample resided in a spatially and chemically equivalent position as the parent sample (Eq. 10) (Chabaux et al., 2013). By satisfying the two variables dt and z for each sample, we calculated the individual weathering age of each sample and then an average WAR_{rind} of the profile. No volume correction was required as the profile weathered isovolumetrically (Fig. S4).

The unknown parameters and WAR_{rind} were constrained using a model that utilizes a non-linear, least-squares problem solving algorithm: the MatLab^{TM} function, *lsqnonlin* (e.g., Chabaux et al., 2011; Dosseto et al., 2014; Ma et al., 2012). The model was solved by minimizing the sum of the squared differences between the known activity ratios, ($^{234}U/^{238}U$) and ($^{230}Th/^{238}U$), and the modeled activity ratios were calculated with a set of random values for the unknowns. A large number of solution sets were iterated (>1,000), with variables constrained by upper and lower boundaries. The final solution set output by the model was the most commonly calculated values of the dataset. Similar algorithms have been successfully used to determine WARs in other studies (Chabaux et al., 2003, 2013; Dosseto et al., 2008, 2012; 2014; Ma et al., 2010, 2012).

2.7 Micro X-ray Fluorescence Spectroscopy (µXRF)

Micro-XRF (µ-XRF) measurements were conducted on the Bisley bedrock thin sections (B1W1-10-5) using the I18 beamline at Diamond Light Source, UK. For the duration of the experiments, the storage ring had operating conditions of 3 GeV electron energy and 150 mA electron current. Standards with known oxidation states for the element of interest were not used, therefore the µXRF maps represent relative proportions of different oxidation states.

Following collimation of the beam, excitation energies were selected using a liquid nitrogen-cooled Si(111) double crystal monochromator. The beam was then focused using non-chromatic Kirkpatrick-baez focusing mirrors to produce a spot size of 2 µm x 2 µm. A 0.1 mm thick aluminum filter was used to reduce the beam current. Samples were mounted at 45^{o} to both the incident beam and a 6-element silicon drift detector (SiriusSD®, SGX Sensortech). All spectra were acquired in fluorescence mode and the distance from the

sample to the detector was adjusted so that that the total count rate was within the range of the processing electronics.

2.7.1 Fe oxidation state maps

Prior to collecting data, the monochromator was calibrated by defining the first derivative peak of an Fe foil standard spectrum as 7112.0 eV with an energy resolution of 0.5 eV at the Fe K-edge. Fe K-edge spectra were recorded using step sizes of 5 eV for the baseline before the edge (6987 – 7099 eV), 0.5 eV for the edge region (7099 – 7137 eV), 1 eV for the XANES region (7137-7150 eV) and 2 eV for energies above 7150 eV. Due to the high concentrations of Fe in the samples, a low dwell time of ~0.1 s per point could be used.

Maps of changing Fe oxidation states were produced by first locating spectral features in XANES that are sensitive to changes in oxidation state. Energies of 7119 eV and 7130 eV were determined for Fe^{2+} and Fe^{3+}, respectively, by comparison of XANES on the edge of a weathered pyrite grain, where oxidation is likely, and the center of an unweathered pyrite grain where oxidation has not occurred or occurred to a lesser extent (Fig. S5). Next, maps of fluorescence intensity as a function of position were produced by rastering the stage both horizontally and vertically for excitation energies of 7080 eV (baseline), 7117 eV (Fe^{2+}), 7130 eV (Fe^{3+}) and 7400 eV (Fe_{total}). Each of the maps were then normalized to the beam intensity (I_0) followed by the subtraction of the baseline map (7080 eV) from each of the other maps. The 7117 eV and 7130 eV maps were then each normalized to the 7400 eV map to account for concentration effects. All data manipulation was performed in Microsoft Excel and the maps produced in PyMca (Software Group, European Synchrotron Radiation Facility).

2.7.2 S oxidation state maps

All experiments were conducted in a helium environment to minimize absorption of the X-rays by air. The monochromator was calibrated by defining the first derivative peak of sulfate within the spectrum of a scotch tape standard (Czapla et al., 2012) as 2472 eV with an energy resolution of 0.3 eV at the S K-edge. Quick XANES were conducted repeatedly on a single grain of pyrite to assess oxidation as a result of beam damage, with no oxidation detected.

Micro-XRF maps of S oxidation states were produced by collecting the S K fluorescence at 2471 eV (S^{1-}), 2482 eV (S^{6+}) and 2600 eV (total fluorescence). The maps were then normalized as per the method described above for Fe µXRF maps. As the oxidation state of S

increases, the absorption edge shifts to higher energies (e.g., Fleet et al., 2005; Métrich et al., 2009; Wong et al., 1984). Therefore, the maximum normalized intensity (a.u.) at each of the energies above can be used to map changing S oxidation states. The S^{2-} peak energy was identified by XANES on a pyrite grain within the sample (Fig. S6). The S^{6-} peak energy was selected from a value for barite in the literature (Métrich et al., 2009) and previous experiments on beamline I18 specifically (Fig. S6).

2.8 Watershed Scale Weathering Advance Rate

When calculating a weathering advance rate at the watershed scale ($WAR_{watershed}$), the rate is normalized to a geographical surface area, as opposed to the mineral grain-scale surface area when calculating WAR_{rind}. In addition, $WAR_{watershed}$ uses stream or river data to calculate mass loss via solute concentration and the time constraint via runoff. As such, $WAR_{watershed}$ provides a contemporary weathering rate for the snapshot moment at which the stream or river is sampled, compared to the kyr timescale represented by WAR_{rind}. By calculating $WAR_{watershed}$ we can therefore compare it to the WAR_{rind} to examine how WAR varies on multiple temporal and spatial scales.

We calculated $WAR_{watershed}$ for the Bisley 1 watershed stream, following the method of Gaillardet et al. (2011):

$$WAR_{watershed} = \frac{CWR}{\varphi_{alk}\rho_p(1-\Phi o)^*} \quad (11)$$

where: φ_{alk} = average mass fraction of alkali and alkaline earth cations per g of parent rock (g g^{-1}); ρ_p = average bulk density of the parent (g cm^{-3}); Φ_o = porosity of the parent material (vol %) and CWR is the cation weathering rate calculated by multiplying the concentration of cations (mg L^{-1}) of the total dissolved solids, TDS_{cat}, by the runoff of the watershed (mm yr^{-1}):

$$CWR = TDS_{cat} * Runoff \quad (12)$$

To calculate $WAR_{watershed}$ using Eq. 11 and 12, daily stream discharge from 2000 to 2005 (Gonzalez, 2011) was used to calculate run off, and weekly chemical composition of the stream and rainfall from 2000 to 2005 (McDowell, 2010; 2012) was used to calculate

rainfall-corrected stream chemistry (raw data from the LTER online database *http://luq.lternet.edu/data)* (Table S1).

To investigate the potential effect of weathering in the Bisley watershed on the global silicate weathering-climate feedback, we used the weekly stream chemistry averaged over five years (Table S1) to determine a CO_2 consumption rate (CDCR) for the watershed (Gaillardet et al., 2011):

$$CO_2\ consumption\ rate = [HCO_3^-] * Runoff \quad (13)$$

where $[HCO_3^-]$ = concentration of HCO_3^- in mol km^{-3} and runoff is in km yr^{-1}. HCO_3^- concentration was calculated from stream chemistry charge balance, as the stream is not hydrothermally impacted, the anionic charge is dominated by HCO_3^-. This equation can therefore also be written as:

$$CO_2\ consumption\ rate = ([Na^+] + [K^+] + 2[Ca^{2+}] + 2[Mg^{2+}]) * Runoff \quad (14)$$

where [i] = concentration in mol km^{-3} and runoff = km yr^{-1}.

3. RESULTS

3.1 Parent rock mineralogy

A Winchester-Floyd plot (Fig. S7) indicates that the original lithology, prior to metamorphism, was an andesite. However, hydrothermal alteration in the area has altered the rock type to an albite-epidote hornfels facies rock, displaying the characteristic hydrothermal minerals: albite, epidote, pyroxene and chlorite. Lower abundance hydrothermal minerals that are present include: pyrite, sphene, illite and apatite. Interestingly, previous work on the lithology of the area (Briggs and Cortes-Aguilar, 1980) marked the Bisley watersheds as outside of the metamorphic aureole of the Río Blanco stock intrusion, however this low-grade, contact metamorphic facies clearly places it within the aureole.

Plagioclase comprises the majority of phenocrysts measuring on average 126 ± 15 µm (determined from SEM images) along the long axis, most of which is albite with occasional intergrowths of anorthite. The albite contains the majority of the bedrock Na, with only trace amounts found in the pyroxene and amphibole. Pyroxene is present as an accessory mineral,

628 predominantly in the form of augite, with variably sized grains from 74 ± 8 μm as
629 phenocrysts to ≤11 ± 3 μm when found in the matrix, with some occasional chloritization. To
630 optimize the signal to noise ratio of the X-ray elemental mapping, a higher accelerating
631 voltage was used during the analysis. The higher accelerating voltage resulted in a greater
632 excitation volume of the parent rock, meaning that due to their size and chemical similarity to
633 augite, amphibole inclusions within the augite grains could not be differentiated. Therefore,
634 the minor amphibole was included in the pyroxene abundances. Epidote has an average grain
635 size of 31 ± 4 μm, with the typical monoclinic-prismatic crystal habit of epidote. Chlorite
636 comprises the majority of the matrix, however as it is microcrystalline, the average grain size
637 was difficult to estimate. Therefore, the mean measurable chlorite grain size for this bedrock
638 of 14 μm reported by Buss et al., (2017) was used (determined from SEM images) and thus
639 the chlorite surface area was likely underestimated.

640 Quartz occurs as an accessory mineral with a fairly homogenous distribution throughout the
641 sample, despite its variable grain size, with 3.0 ± 0.9 μm sized grains, on average, for those
642 that were measurable. In addition, microcrystalline quartz comprises part of the matrix, but
643 these grains were too small to measure on the SEM. Evidence of hydrothermal alteration
644 includes occasional quartz veins and sphene, illite, apatite and pyrite. Sphene occurs within
645 the matrix, concentrated around the edges of larger grains. Illite occurs as a component of
646 minor sericitization of plagioclase grains (Fig. 2A). Apatite resides within the matrix as
647 small, spherical/sub-spherical grains constituting the only measurable source of phosphorous.
648 The distribution of pyrite is heterogeneous within the rock, with grains of 14 ± 2 μm in size.
649 Trace barite, arsenopyrite and chalcopyrite also occur.

650

651 **3.2 Weathered mineralogy and profiles**

652 The order in which the onset of mineral dissolution occurs can be estimated from the depth of
653 each mineral's weathering reaction front (Fig. 3 and 4) and SEM observations. Using this
654 method, the order of mineral dissolution was found to be: pyrite > pyroxene > chlorite >
655 anorthite > illite ≈ apatite > albite ≈ epidote. Quartz and sphene are conserved across the
656 profile. Incipient pore space is frequently lined with Mn-oxide (MnO_2) precipitates around
657 the edges (Fig. 2B). Chlorite is the only primary mineral found to contain Mn and this is in
658 trace amounts (Table 1). Gibbsite and kaolinite were also commonly found within pore space,

659 but they formed less thorough linings than the Mn-oxides (Fig. 2C). Anorthite concentrations
660 were very low, with large uncertainties.

661 Fe(III)-(hydr)oxides, kaolinite and gibbsite all increase from ~35 mm inboard of the fracture
662 surface (Fig. 4F, 4G and 4H), with a sharp increase from ~8 mm in the case of kaolinite and
663 Fe(III)-(hydr)oxides and ~6 mm for gibbsite. The sharp increase in kaolinite at ~8 mm from
664 the fracture surface is coincident with losses of Na from albite increasing at the same point
665 (Fig. 5D). BSE images show the presence of pitting within albite grains (Fig. 2D).

666

667 **3.3 Major element profiles**

668 The calculations of volumetric strain (Fig. S4) suggest that Si, Al and Ti are largely
669 conserved (immobile) within the weathering profile. However, when τ was calculated for Si
670 and Al, with Ti as the immobile (Fig. S8A), they both showed slight relative losses compared
671 to parent material. Conversely, when τ was calculated for Ti with either Al or Si immobile
672 (Fig. S8B and S8C), Ti showed enrichment. Therefore, Ti is likely more immobile than Al
673 and Si in the Bisley bedrock weathering profile.

674 The bulk elemental concentrations were measured by ICP-OES to support the elemental X-
675 ray mapping data, and the values agree remarkably well (Figs. 5 and 6A-D). However, due to
676 the larger uncertainties associated with the ICP-OES data, we used the elemental X-ray
677 mapping data for all calculations and data analysis.

678 Calculations of the mass transfer coefficient using Ti ($\tau_{Ti,j}$) (Eq. 2, presented in Figs. 5 and 6)
679 were used to determine the depth at which depletion begins for each element. From these
680 depths, the order of cation mobility from the parent material, through the weathered rind, and
681 to the fracture surface was determined as: Ca>Mg>Na≈Si≈Al, with Fe conserved within the
682 rind. Due to the high uncertainty associated with the low K and S concentrations and their
683 heterogeneous distribution, it was not possible to make meaningful interpretations from their
684 profiles and they are therefore not presented. The most substantial loss was shown by Ca,
685 beginning at ~50mm, where 30% of the element was lost over 15 mm (Fig. 5B) with a final
686 loss of 60% over the final 10 mm, resulting in a total depletion of ~ 90% for Ca ($\tau_{Ti,Ca}$ = -
687 0.90). There is no significant loss of Mg within the weathering profile, until the shallowest
688 ~20 mm where a gradual loss up to the fracture surface totals ~45% ($\tau_{Ti,Mg}$ = -0.45) (Fig.

5C). Na, Si and Al all display a similar trend of conservative behavior over the majority of the profile until the visible rind (0-6 mm from the fracture surface) where they reflect losses of ~60 % ($\tau_{Ti,Na}$ = -0.57), ~45 % ($\tau_{Ti,Si}$ = -0.47) and ~40% ~60 % ($\tau_{Ti,Al}$ = -0.47), respectively. These losses correspond to losses of albite, which occurred over the same depth (Fig. 3B).

3.4 Porosity development and density changes

Porosity (Φ) remains close to zero from 56.5 mm (the sample furthest inboard of the fracture surface) to roughly 40 mm from the fracture surface (Fig. 7). At this point it gradually increases by ~2-3 vol% until <10 mm from the fracture surface where a significant increase in porosity was observed across the weathering front and into the rind. A maximum Φ of 15.0 ± 3 vol% was reached within the rind. This porosity is the same within uncertainty as the neutron scattering porosity of 8 ± 4 vol% measured on the weathered Bisley rock (Buss et al., 2013).

Rock density was calculated using mineral density values taken from the literature (Table 1), and mineral volumes observed using X-ray phase analysis. Density calculated in this way yielded a value of 2.9 g cm^{-3} for the parent material and 2.2 g cm^{-3} for the rind material, compared with a bedrock density of 2.3 g cm^{-3} as measured by volume displacement (Buss et al., 2017). When normalized to the parent material density, very little change was noted in the weathered material density across the profile (Fig. 7) except in the weathering rind, where the density ratio increased to ~1.24.

3.5 Oxidation within pores

The oxidation state of Fe in an unweathered pyrite grain at ~55 mm from the fracture surface, is +2 (Fig. 8A), as expected. The oxidation state of Fe in the surrounding weathered chlorite grain is +3. There is also no definitive sign of Fe retention within pores. Sulfur within the pyrite has an oxidation state of -2 (Fig. 8B), as expected, with no other minerals in the map boundaries bearing any sulfur. X-ray phase analysis indicated that there is sulfur within the pore space (Fig. 2E) in association with secondary minerals such as kaolinite and gibbsite; μXRF indicated that this is oxidized sulfur (+6).

719

720 **3.6 U-Th mobility and activity ratios**

721 The unaltered parent material has U and Th concentrations of 0.83 ppm and 1.26 ppm,
722 respectively (Table 2). The U concentration is comparable to previous work on a landslide-
723 exposed outcrop of Bisley bedrock (Dosseto et al., 2012) whereas the Th concentration
724 reported here is higher. Th is conserved throughout the profile (Fig. 6E), relative to the
725 immobile component (Ti). However, the $\tau_{Ti,Th}$ profile displays two outliers at 10.5 mm and
726 13.5 mm from the fracture surface, which contain anomalously high concentrations of Th
727 relative to the parent material. We found that U is conserved throughout most of the profile,
728 except for a slight enrichment of ~5% at ~20 mm from the fracture surface and a loss over the
729 visible rind of ~8-9% (Fig. 6F).

730 If the hydrothermal activity that occurred in the area ~60 Ma (Smith et al., 1998) altered the
731 U-series activity ratios, sufficient time has passed (>1.3 Myr) for secular equilibrium to be
732 reached. Values of ($^{234}U/^{238}U$) are significantly greater than 1 across the entirety of the
733 transect (Table 2 and Fig. 9A), with an increase toward the rind compared to the deeper 7
734 samples. The furthest sample inboard of the fracture surface (46.5 mm) also shows higher
735 activity ratios, similar to the rind. Starting from close to secular equilibrium at the furthest
736 sample inboard of the fracture surface, the ($^{230}Th/^{238}U$) ratios (Table 2 and Fig. 9B) show an
737 increase >1 with decreasing distance from the fracture surface. Samples at 16.5 mm and 4.5
738 mm from the fracture surface are exceptions to this, with values slightly less than 1. An
739 outlier exists with a ($^{230}Th/^{238}U$) ratio of 1.097 at 10.5 mm inboard of the fracture surface,
740 which also shows an increase of 50% in the $\tau_{Ti,Th}$ profile, relative to the parent material (Fig.
741 6E).

742 **3.7 Weathering advance rate at the rind scale**

743 The U-Th nuclide loss/gain model provided weathering exposure ages across the weathering
744 profile (Table 3), with the outermost rind sample having a weathering age of ~3.2 kyr. The
745 mean weathering age of the profile is 1264 years. Using the mean weathering age, the
746 transect length (46.5 mm) and Eq. 10, a WAR_{rind} of 37 ± 2 mm kyr^{-1} was derived. No
747 volumetric correction was required as isovolumetric weathering was assumed, which was
748 reasonable because the volumetric strain values were near zero (Fig. S4) and SEM

observations indicated retention of the original mineral structures within the rind (Fig. 2G). The model yielded a k_{234}/k_{238} ratio of 0.88.

3.7 Mineral-specific weathering rates

Here we present mineral-specific dissolution rates (Eq. 5; Tables 1 and 4) for the notable primary minerals excluding quartz (which is conserved), using the calculated WAR_{rind} (Eq. 10) as a time constraint and the gradients as shown in Fig. 10. Mineral gradients were calculated over the distance where each mineral shows pronounced losses, which for all minerals spans the visible rind and extends several mm deeper, as observed in the normalized mineral profiles (Fig. 10). We also calculated additional, deeper gradients for the early stage dissolution of both chlorite and pyroxene (Fig. 10D-E). Although albite and epidote show variation in their gradients inboard of the rind, SEM observations indicate that these result primarily from heterogeneities within the rock, not weathering, and have therefore not been included in the calculation of the gradients for these minerals.

We calculated a pyrite dissolution rate (Eq. 5) of $1.8 \times 10^{-12} \pm 2.4 \times 10^{-15}$ mol m^{-2} s^{-1} ($\log r_m$= -11.8) from the only clear gradient, which spans the visible rind, although evidence for dissolution of pyrite is apparent in SEM and µXRF maps further inboard of the fracture (55 mm; Fig. 10). The dissolution rate determined for pyroxene from the deepest gradient (~50-60 mm inboard of the fracture surface), is $6.9 \times 10^{-13} \pm 2.3 \times 10^{-15}$ mol m^{-2} s^{-1} ($\log r_m$ = -12.2). Across the visible rind, the dissolution rate of pyroxene was calculated as $1.5 \times 10^{-12} \pm 4.8 \times 10^{-15}$ mol m^{-2} s^{-1} ($\log r_m$ = -11.8), we derived dissolution rates for chlorite of $1.0 \times 10^{-14} \pm 1.3 \times 10^{-16}$ mol m^{-2} s^{-1} ($\log r_m$ = -13.9) from the deepest gradient (~40-50 mm inboard of the fracture surface) and $2.9 \times 10^{-14} \pm 3.8 \times 10^{-16}$ mol m^{-2} s^{-1} ($\log r_m$ = -13.5) from the gradient that spans the weathering rind, Albite and epidote dissolution rates of $1.1 \times 10^{-12} \pm 2.9 \times 10^{-14}$ mol m^{-2} s^{-1} ($\log r_m$ = -12.0) and $4.3 \times 10^{-13} \pm 1.4 \times 10^{-15}$ mol m^{-2} s^{-1} ($\log r_m$ = -12.4), respectively, were calculated across the rind.

3.8 Weathering advance rate at the watershed scale

Using the stream chemistry data in Table S1 plus Eq. 11 and 12, we calculated a $WAR_{watershed}$ of 39 ± 9 mm kyr^{-1} following the method of Gaillardet et al. (2011). From the stream

chemistry data (Table S1) and using Eq. 13 or 14, the CO_2 consumption rate (CDCR) for the Bisley watershed was calculated to be ~ 1029 x 10^3 ± 320 x 10^3 mol km^{-2} yr^{-1}.

4. DISCUSSION

4.1 Weathering reactions

The albite-epidote hornfels bedrock of the Bisley watershed weathers at a rate of 37 ± 2 mm kyr^{-1} with between 40-90% of each cation lost over the mm-scale profile. The first mineral to weather is pyrite via oxidation, followed by pyroxene > chlorite > anorthite > illite ≈ apatite > albite ≈ epidote. The order of mineral dissolution given in Section 3.2 does not follow the order predicted by the Goldich dissolution series, suggesting that the system cannot be described simply by mineral crystal stability alone. The oxidation of Fe(II)-bearing minerals has previously been identified as the incipient weathering reaction in other lithologies in different watersheds, including the adjacent granitic watershed of Río Icacos (Buss et al., 2008) and other granitic watersheds in Virginia, USA (Bazilevskaya et al., 2015) and California, USA (Goodfellow et al., 2016); the Susquehanna Shale Hills CZO in central Pennsylvania, USA (Brantley et al., 2013); and a charnockitic profile in Sri Lanka (Behrens et al., 2015). Pyrite oxidation as the incipient reaction has also previously been proposed for the Bisley bedrock (Buss et al., 2013) and is demonstrated here by evidence of S oxidation within pores (Fig. 8B).

Although losses in pyrite content between 60-50 mm from the fracture surface are within the variability of the parent material, SEM-BSE imaging (Fig. 2F and H) suggest that the dissolution of pyrite is the first weathering reaction (furthest inboard of the fracture surface). In areas of early-stage pyrite dissolution identified by SEM-BSE, µXRF maps (Fig. 8) show that pyrite dissolution occurs with oxidation of S, consistent with sulfuric acid production. Following the dissolution of pyrite, pyroxene and chlorite dissolve earlier than albite and epidote (Fig. 3B-E). The earlier onset of pyroxene and chlorite dissolution could be due to several reasons: i) pore water is more undersaturated with respect to pyroxene and chlorite than to epidote and albite; ii) pyrite occurrences (which dissolve first creating incipient porosity that allows greater access of reactive fluids) are more closely associated with pyroxene and chlorite; and iii) the products of oxidative pyrite dissolution act to catalyze the dissolution of pyroxene and chlorite.

As the elements contained within epidote are also present in chlorite and pyroxene, it is unlikely that the saturation state of the pore water with respect to pyroxene and chlorite would be appreciably different to the saturation state with respect to epidote. It is possible that pyroxene is more accessible following pyrite dissolution due to its higher correlation with pyrite abundance (r^2= 0.57, p <0.01, Fig. S9B), however albite also shows a moderately high correlation (r^2= 0.47, p <0.01, Fig. S9C); epidote content is not well correlated with pyrite (r^2= 0.19, p >0.01, Fig. S9D) and chlorite shows the least correlation (r^2= 0.12, p >0.01, Fig. S9A), suggesting this is not the primary cause for the earlier onset of pyroxene and chlorite dissolution. Finally, there is evidence of oxidative dissolution of pyrite from μXRF analysis of S oxidation states within a pyrite grain and pore space (Fig. 8B). Pyrite dissolution in the presence of oxygen generates acidity (Eq. S1), which would create a low-pH microenvironment on a mineral grain scale. It is possible that ferrous iron liberated in this reaction would then oxidize to ferric iron, which could then catalyze further pyrite dissolution and sulfur oxidation. However, from the μXRF data (Fig. 8A) there is no evidence that Fe^{3+} is retained within pores to catalyze the reaction. Regardless of whether or not Fe^{3+} acts as a catalyst, the oxidation of pyrite still produces H^+, promoting dissolution of other minerals in the vicinity of pyrite grains, consistent with our observations in the Bisley rock (e.g., Fig. 2F and H).

Once minerals surrounding a pyrite grain have dissolved and created pore space, the second possibility for earlier dissolution of pyroxene and chlorite, where reactive fluids are better able to penetrate the rock, could become important. A dual-stage mechanism such as this is reflected in the τ profile for Ca (Fig. 5B) where there is an initial loss much further inboard than the loss over the visible rind. Anorthite dissolution may also contribute to the initial increase in porosity between 40-30 mm (Fig. 8); however, the majority of porosity development occurs in the visible rind (increase of about 13% over the outer 6 mm), several cm distant from where anorthite dissolution was completed.

Pyroxene near pyrite grains is observed to dissolve second (Fig. 2H), and the pyroxene and pyrite abundances show the highest correlation (r^2= 0.57, Fig. S9B). Therefore, initial pyroxene dissolution is expected to occur largely via attack by sulfuric acid (Eq. S2) produced by the oxidative dissolution of pyrite, as observed in SEM-BSE imaging and EDS analysis. Closer to the rind, as the supply of pyrite dwindles, the porosity increases, and fresh reactive fluids are better able to penetrate, it is likely that the dissolution of pyroxene will

proceed at a higher pH via protons sourced dominantly from carbonic acid (Eq. S3) present in the infiltrating fluids.

Chlorite is the next mineral to dissolve, at a similar depth to the oxidation of pyrite, the dissolution of pyroxene, and formation of kaolinite as observed by SEM (Fig. 2C). Both albite and epidote abundances show a higher correlation with pyrite than chlorite does with pyrite (r^2 = 0.47, 0.19 and 0.12, respectively; Fig. S9), suggesting that it may not be close association with pyrite that is the critical factor, but the mineral's susceptibility to sulfuric acid promoted dissolution. The depth of the chlorite weathering front is in fact concurrent with the depth of pyrite oxidation and the susceptibility of chlorite to attack via sulfuric acid, following the oxidation of trace pyrite, has previously been reported within the Marcellus shale, USA (Heidari et al., 2017). Thus, we propose that chlorite dissolves via analogous reaction mechanisms to those described for pyroxene, sulfuric acid- or carbonic acid-promoted dissolution (Eq. S4 and Eq. S5, respectively) with the subsequent production of kaolinite. Both albite and epidote dissolve primarily over the rind where the carbonic acid reaction mechanism dominates (Eq. S6 and Eq. S7, respectively).

As mentioned in Section 3.2, pore space is frequently lined with Mn-oxide precipitates between 48 mm and 10 mm from the fracture surface. The substantial MnO_2 accumulations lining the pores (Fig 2B) may lower the total reactivity of the rock, slowing the WAR by denying infiltrating fluids access to fresh primary minerals. Mn-oxides are also effective scavengers of metals, acting to retain dissolved cations within pores via adsorption (e.g., Peacock et al., 2012; Taylor and McKenzie, 1966; Vuorinen and Carlson, 1985). In the Bisley rocks, inhibition of weathering by Mn-oxides would occur only from 40 – 10 mm distance from the fracture surface (Fig. 4E), where at 10 mm MnO_2 is removed from the pores, likely due to increased fluid flux in the advection dominated rind.

From the evidence above for a two-stage weathering mechanism: first by reaction with sulfuric acid in the fresh rock, followed by reaction with carbonic acid in the rind, it is likely that the initial reaction of pyrite oxidation controls the onset of chemical weathering. In turn, the dissolution of pyrite in the Bisley bedrock is regulated by the concentration of an oxidizing reactant such as O_2 (Buss et al., 2013; 2017), therefore the diffusion rate of oxygen into the bedrock is likely the rate-limiting step. If pore water oxygen concentration is the rate-limiting factor, this could regulate a steady-state weathering profile at the regolith scale.

Because O_2 concentration decreases with depth in the Bisley regolith (measured at a nearby site; Buss et al., 2017), then as the WAR increases and the regolith thickens, the O_2 concentration at the bedrock-regolith interface decreases. In turn, the decreased O_2 concentration causes the WAR to slow, allowing surface erosion to thin the regolith and increase O_2 at the bedrock-regolith interface again (Fletcher et al., 2006). The multiple mechanisms described above (i.e., oxidative weathering of pyrite and weathering of other minerals by both sulfuric and carbonic acid) suggests that the Bisley bedrock has at least two weathering fronts. These weathering fronts likely progress at different rates and therefore the WAR_{rind} calculated here would reflect an average.

4.2 Comparison of mineral-specific weathering rates

Field-measured mineral dissolution rates are not simply kinetic-controlled rates as are many laboratory determined rates, instead they reflect a multitude of variables, including the saturation index of reactive fluids with respect to the mineral of interest (e.g., Zhu et al., 2004), past climatic conditions (e.g., Nagarajan et al., 2014), varying redox conditions (e.g., Fletcher et al., 2006), microbial activity (e.g., Balogh-Brunstad et al., 2008) and the accessibility of the mineral within the rock to reactive fluids (e.g., Navarre-Sitchler et al., 2009). The accessibility of the mineral, in turn, depends on multiple controls including the dissolution rate of neighboring minerals (to create porosity) and the degree to which the resulting pores are then lined with secondary phases, such as kaolinite and Mn-oxides. Most of the weathering observed in thin sections was physically inaccessible to microorganisms (too small or disconnected pore space), although microbial activity in overlying regolith likely affects the reactivity of the pore fluids infiltrating the rock (e.g., by producing CO_2, consuming O_2, oxidizing Fe(II) or other redox active elements).

The complex nature of natural dissolution rates is highlighted in this study by the case of pyrite. Buss et al. (2013) previously proposed that the formation of the entire critical zone of the Bisley watershed is controlled by rind formation, which in turn is controlled by pyrite dissolution. This dissolution rate ($\log r_m$ = -11.8, Fig. 11) is several orders of magnitude slower than laboratory determined rates ($\log r_m$ = -4.55, Fig. 11). Faster laboratory rates could be due to various issues such as pre-experimental cleaning processes, higher surface area and higher water:mineral ratios that exist in laboratory experiments compared to field settings

(White and Brantley, 2003). The calculated pyrite dissolution rate presented here also matches a previously determined field dissolution rate for pyrite (log r_m = -11.7, Fig. 11). España et al. (2007) found that laboratory oxidation rates of Fe(II) in pyrite (10^{-8} to 10^{-10} mol L^{-1} s^{-1}) were 2-3 orders of magnitude slower than field determined dissolution rates (10^{-6} to 10^{-7} mol L^{-1} s^{-1}), due to the influence of microbial oxidation on the field rates; this is the inverse of the field-laboratory discrepancy typically observed for silicate dissolution rates. However, microbial activity in the field will depend on the community present and factors including temperature, pH and nutrient availability. Indeed, Choppala et al. (2017) found that biotic oxidation had only a minor contribution in field-settings, concluding that pyrite oxidation rates are surface area dependent, a relationship often assumed to be linear (Lowson, 1982). The relationship between pyrite dissolution rates and mineral surface area is complicated by the non-uniform attack of oxidants (Bierens de Haan, 1991), which occurs at sites of high excess surface energy (e.g., etch pits, defects and grain edges; McKibben and Barnes, 1986). Pyrite oxidation can also vary with grain-size (Gartman and Luther, 2014) whereby during a later stage of oxidation, electron shuttling occurs across the mixed valence oxide coating of smaller grains; larger particles form an oxygen-limiting, armor coating. Most studies do not account for this when crushing large grains to examine the oxidation of small grains (Gartman and Luther, 2014). The slower than expected oxidation rate of smaller particles, could explain why the pyrite dissolution rate for Bisley grains (~ 14 μm) is several orders of magnitude slower than lab-determined dissolution rates.

The initial dissolution rate of pyroxene (log r_m = -12.2, Table 4) and the dissolution rate over the rind (log r_m = -11.8) are both more than an order of magnitude faster than pyroxene dissolution rates previously determined within a basalt from another tropical catchment in Paraná, Brazil (Fig. 11). The pyroxene dissolution rates presented here agree well with the experimental rates reported in Palandri and Kharaka (2004) (Fig. 11) for near neutral pH.

The dissolution rate derived for chlorite over the weathering rind (log r_m = -13.5, Table 4, Eq. S5) is similar to that calculated in the deep regolith of this watershed (log r_m = -13.1; Fig. 11) and those experimentally-determined (log r_m = -12.52; Fig. 11). Buss et al. (2017) used Mg fluxes to estimate chlorite dissolution rates for the Bisley watershed, assuming congruent dissolution. Therefore, the slight discrepancy between their faster dissolution rates and the one calculated here based on direct observation of chlorite abundances, may indicate incongruent weathering of chlorite with preferential loss of Mg occurring during the earlier

935 stages. In addition, the high porosity of the regolith (60 vol%; Buss et al., 2017) compared to
936 the rinds (15 vol%) and non-rind rocks (0.5 vol%) allows better access of reactive fluids to
937 the weathering minerals. Furthermore, the molecular mechanism of chlorite dissolution may
938 also lead to faster regolith chlorite weathering. Lowson et al. (2007) describes clusters of
939 partially hydrolyzed silica tetrahedra remaining on chlorite surfaces following initial proton
940 attack of the Al tetrahedral sites during dissolution. The rate-defining step of chlorite
941 dissolution is the conversion of these hydrolyzed silica species (via a precursor) into an
942 aqueous silica species (Lowson et al., 2007). Therefore, the chlorite dissolution rate will be
943 controlled by the concentration of aqueous Si in porewater, which may be more dilute in
944 regolith than in rinds due to faster water flow.

945 Both the pyroxene and chlorite dissolution rates calculated here in the presence of sulfuric
946 acid are slower than those rates calculated for the same minerals in the presence of carbonic
947 acid (Fig. 11; Table 4, Eq. S2-S5). Contrary to this observation, chlorite has previously been
948 modeled to weather faster in association with sulfuric acid than carbonic acid within a shale
949 bedrock (Heidari et al., 2017). However, the mineral dissolution rates presented here would
950 be controlled by the supply of sulfuric acid, which is limited by the oxidative dissolution rate
951 of pyrite. The oxidative dissolution rate of pyrite in this study is several orders of magnitude
952 slower than those previously determined in the literature, suggesting that this rate is also
953 supply-limited, consistent with the low abundance of pyrite as well as the hypothesis that the
954 diffusion of oxygen into the bedrock is the rate-limiting step in weathering of the Bisley
955 bedrock.

956 The plagioclase (albite) dissolution rate calculated here (log r_m = -12.0, Fig. 11, Table 4, Eq.
957 S6) is an order of magnitude faster than that calculated for plagioclase (50:50 albite:anorthite)
958 in the neighboring granitic watershed (log r_m = -13.0; Buss et al., 2008). Our albite
959 dissolution rate agrees well with lab determined rates (Fig. 11). Our field-determined epidote
960 dissolution rate (log r_m = -12.4, Fig. 11, Table 4, Eq. S7) is faster than experimental rates (log
961 r_m = -14.9 and -16.20; Sverdrup, 1990; Kalinowski et al., 1998, respectively), despite a
962 similar pH range (lab: 5.5 to 4.5, Bisley regolith porewater: 4.4 to 5.7; Buss et al., 2017).

963 The low pH of the Bisley regolith porewater (4.7; Buss et al., 2017), and the high dissolution
964 rates reported here, may reflect the low pH microenvironment produced by the oxidative
965 dissolution of pyrite. The pH necessary to produce the dissolution rates here can be estimated

by rearranging the pH dependent linear rate equation presented by Palandri and Kharaka (2004). All of the minerals except pyrite and pyroxene would require a pH of 4.6-5.6 (Table S2), agreeing well with the measured pH of the Bisley porewater. The higher pH required for pyrite (pH = 8.6) is unsurprising as its dissolution is independent of pH and would be controlled instead by the concentration of oxidants. However, this would not explain the higher pH required to dissolve pyroxene both initially (pH = 7.7) and over the rind (pH = 7.1). It is more likely that each minerals dissolution rate varies due to more parameters than just pH dependence.

The much higher mineral dissolution rates calculated here, compared to other published field-calculated dissolution rates from other locations are not surprising, considering that the tropical temperatures and abundant rainfall in the Luquillo rainforest make fast dissolution rates thermodynamically favorable. As a result, a large proportion of the primary minerals (~80% pyroxene, ~50% albite, ~40% epidote and ~30% chlorite) are lost over only several mm's of weathering rinds. The precise balance of transport mechanisms (between diffusion and advection) are uncertain in the Bisley bedrock, however, as such thin reaction fronts are considered diagnostic of a diffusion dominated transport system (Lebedeva and Brantley, 2013; Ma et al., 2011; Navarre-Sitchler et al., 2009; 2011; 2013), we assume diffusion is the primary mode of transport in the rinds. Field-calculated mineral dissolution rates that match or exceed laboratory dissolution rates are rarely observed; instead mineral dissolution rates determined in the field are usually 2-5 orders of magnitude *slower* than those determined in the laboratory (e.g., White and Brantley, 2003). Slower field-calculated dissolution rates have previously been ascribed to the presence or absence of organic acids (Drever and Stillings, 1997; Lawrence et al., 2014); armoring of mineral surfaces (Nugent et al., 1998); physical erosion of weathered material influencing interpretations (Bluth and Kump, 1994) or supersaturation of the pore fluid due to slow precipitation of secondary minerals (e.g., Zhu et al., 2004). If the discrepancy between lab and field dissolution rates is an issue of fluid saturation (and therefore describes a transport-limited system), then fluid residence time may be the rate-limiting step (Maher, 2010). Alternatively, local grain-scale roughness may provide the main control on dissolution rates in weathering rinds (Sak et al., 2010). However, roughness is dependent upon the measuring resolution at the scale of interest and as such, the grain-scale surface area is difficult to estimate for field systems (Navarre-Sitchler et al.,

2011), necessitating a fractal dimension to calculate appropriate surface areas (Navarre-Sitchler and Brantley, 2007).

The mineral dissolution rates presented here, which converge with lab-determined rates, demonstrate the importance of the spatial scale of analysis. Calculating mineral dissolution rates only over the mm-scale at which they occur i) avoids underestimation of dissolution rates by over-scaling (i.e., averaging over meters or kilometers); ii) minimizes the effects of other Earth surface processes such as physical erosion and organic acid production, as the thick Bisley regolith likely decouples many deep and surface processes (e.g., Buss et al., 2013; 2017); iii) circumvents temporal scaling issues associated with exposure time, such as armoring of mineral surfaces, as the dissolution rate is calculated at the weathering front where mineral surfaces are still fresh; and iv) allows normalization to the dissolving mineral's surface area in a similar fashion to laboratory calculated rates. It is therefore expected that by accounting for spatial and temporal scaling issues, field calculated dissolution rates should be similar to those calculated in laboratory studies.

4.3 Uranium-series isotope behavior across the weathering profile and the weathering advance rate across the rinds (WAR_{rind})

U/Th isotope disequilibria data was gathered in this study to model weathering ages of the rock and calculate a WAR_{rind}, which was used to determine the mineral-specific dissolution rates, and to compare to WAR calculated at the watershed scale. Analysis of the U and Th isotope ratios within the weathering profile not only enabled modeling of chemical weathering ages, but also revealed insights into the behavior of these isotopes during weathering rind development.

Activity ratios of ($^{230}Th/^{238}U$) are ~1 (i.e., secular equilibrium) throughout most of the profile, suggesting no net loss or gain of ^{238}U or ^{230}Th (Fig. 9B). However, within the top of the profile $^{230}Th/^{238}U \neq 1$, reflecting greater mobility. This is consistent with the $\tau_{Ti,U}$ profile, which shows losses over the visible rind (Fig. 6F) and the $\tau_{Ti,Th}$ profile (Fig. 6E), which shows Th to be conserved. All ($^{234}U/^{238}U$) activity ratios throughout the sampled profile are >1, suggesting a gain of ^{234}U (Fig. 9A). These observations can all be reconciled if the system is not simply described by U loss, but with U addition as well, where an overall loss of U occurs (as evidenced by $\tau_{Ti,U}$ profile), but there is an addition of ^{234}U relative to ^{238}U, as evidenced by the increased ($^{234}U/^{238}U$) ratios (Fig. 9A and Table 2), whilst ^{230}Th is

conserved, as evidenced by the (^{230}Th/^{238}U) profile (Fig. 9B and Table 2) and the $\tau_{Ti,Th}$ profile (Fig. 6E). The outlier at 10.5 mm depth, displaying an enrichment of Th of ~50% in the $\tau_{Ti,Th}$ profile (Fig. 6E), and the highest (^{230}Th/^{238}U) activity ratio in the profile (Fig. 9B and Table 2), may reflect an infiltration of Th-rich hydrothermal fluids associated with the intrusion of the Rio Blanco stock intrusion near the study site.

It is likely there would be a greater addition of ^{234}U than ^{238}U from an external source, as it is a more soluble nuclide. At greater depths than the visible rind, fluid circulation through micro-fractures may have added ^{234}U to the system, without sufficient weathering to liberate U from the minerals. A more likely explanation is that U leaching has occurred concurrently to ^{234}U addition, but to a lesser extent. Sheng and Kuroda (1986) suggest that a phase may eject ^{234}U into a less soluble phase as a result of alpha recoil, then when it is preferentially dissolved over the less soluble phase, the system's (^{234}U/^{238}U) would be >1. All of these possibilities imply that mineral-water interaction has occurred throughout the entirety of this profile. The interpretation of weathering throughout the U-series sampled profile is supported to some degree by the CIA and τ profiles (Fig. 5 and 6), both of which track weathering deeper into the rock than the U-series profiles. Our calculated average WAR_{rind} of 37 ± 2 mm kyr^{-1} (Eq. 10) is two orders of magnitude faster than those calculated for basalt weathering rinds in other tropical locations (e.g., Ma et al., 2012; Pelt et al., 2008) and an order of magnitude slower than for andesites calculated on a watershed scale (Rad et al., 2013). To our knowledge, there are no other weathering advance rates for andesitic rinds in the tropics in the literature.

4.4 Weathering advance rates across multiple scales

The $WAR_{watershed}$ calculated here of 39 ± 9 mm kyr^{-1} is within error of the calculated WAR_{rind} of 37 ± 2 mm kyr^{-1}. The agreement in WAR between the rind and watershed scales has three key implications: Firstly, weathering solute fluxes of the Bisley 1 stream are dominated by weathering along bedrock fractures. This observation is supported by A) Chapela Lara et al. (2017), who estimated that during base flow, 84% of the Mg dissolved in the Bisley 1 stream originates from the dissolution of bedrock chlorite; and B) Schellekens et al. (2004) who find that after heavy rainfall there is a rapid streamflow response in the watershed that is dominated by fast, near-surface flow paths, highlighting the interconnectivity between bedrock fractures and the stream. The second implication is that the WAR across the whole

watershed is constant, from the watershed scale (6.7 km^2) down to the rind scale (<5 mm), supporting Hynek et al. (2017), who found that regularly distributed fractures in the Bisley bedrock promotes relatively homogenous weathering rates across the watershed. The third and most intriguing implication relates to the difference in timescale between WAR_{rind} and $WAR_{watershed}$. The $WAR_{watershed}$ is calculated from dissolved ions for the moment in time at which sampling took place (here from 2000-2010), thus recording the contemporary WAR, whereas the bedrock weathering profile took a maximum of 4.2 ± 0.3 kyr to form, recording a longer-term, average WAR. For both the $WAR_{watershed}$ and WAR_{rind} to return roughly equal values suggests that the watershed has been in a weathering steady-state for at least the maximum exposure age recorded (4.2 ± 0.3 kyr).

The weathering advance rate for the regolith ($WAR_{regolith}$) of the Bisley catchment calculated by Dosseto et al. (2012) at site B1R (Fig. 1), is 334 ± 46 mm kyr^{-1}, calculated over ~16 m. The $WAR_{regolith}$ (m-scale) represents an intermediate spatial scale between the $WAR_{watershed}$ (km-scale) and WAR_{rind} (mm-scale), however the regolith has been exposed to reactive fluids for 60 kyr (Dosseto et al., 2012), a longer period of time than the bedrock fractures and rinds, and thus also represents an older record of weathering. A $WAR_{regolith}$ that is an order of magnitude faster than the calculated $WAR_{watershed}$ and WAR_{rind} suggests that weathering occurred at a much faster rate in the Bisley 1 watershed prior to the oldest rind exposure age of 4.2 kyr. Previous paleoclimatic work suggests that the Caribbean was wetter and warmer during the mid-Holocene (~6-5 kyr) than the present day (Hodell et al., 1991; Mayewski et al., 2004), which would encourage a faster WAR. Another possibility is that the weathering processes within the bedrock (represented by WAR_{rind} and $WAR_{watershed}$) are *spatially* decoupled as well as temporally from the weathering processes with the regolith.

To place the chemical weathering in the Bisley watershed in a global context, we also estimated its current effect on the global carbon cycle by calculating a CO_2 consumption rate (CDCR) of ~ 1029 x 10^3 ± 320 x 10^3 mol km^{-2} yr^{-1} from stream water chemistry (Eq. 14). This rate is comparable to others calculated for Caribbean watersheds, such as those on Guadeloupe, with a median of ~1300 x 10^3 mol km^{-2} yr^{-1} (Gaillardet et al., 2011) and on Dominica, with a range of 500 to 1500 x 10^3 mol km^{-2} yr^{-1} (Goldsmith et al., 2010). If streams from tropical watersheds are compared to CDCR values calculated by Gaillardet et al. (1999) of major rivers in temperate latitudes such as 226 mol km^{-2} yr^{-1} (Seine) and 542

mol km^{-2} yr^{-1} (Rhine), it is evident that weathering in small tropical watersheds represents a significant component of the global carbon cycle.

5. Conclusions

The meta-volcaniclastic, albite-epidote hornfels bedrock in the Bisley watershed weathers rapidly along deep subsurface fractures with the vast majority of primary minerals lost over several mm's within the weathering rinds that form along fracture surfaces. The rate of primary mineral dissolution is accelerated via the dissolution of accessory pyrite, lowering the pH of porewater within the rock, despite pyrite only comprising ~0.5 vol% of the parent material. Pyroxene and chlorite are particularly susceptible to this reaction, dissolving in the presence of sulfuric acid at rates of log r_m = -14.0 and -12.2 mol m^{-2} s^{-1}, respectively. Then pyroxene and chlorite dissolve within the rind in the presence of carbonic acid at rates of log r_m = -11.8 and -13.5 mol m^{-2} s^{-1}, respectively. Albite and epidote also dissolve more readily within the rind in the presence of carbonic acid, at rates of log r_m = -12.0 and -12.4 mol m^{-2} s^{-1}, respectively.

The $WAR_{watershed}$, which records contemporary weathering rates, and WAR_{rind}, which records kyr-averaged weathering rates, are within error of each other (39 ± 9 mm kyr^{-1} and 37 ± 2 mm kyr^{-1}, respectively). The similarity in WAR calculated on these differing spatial and temporal scales suggests that the Bisley watershed has been weathering in steady-state for a minimum of ~4.2 ± 0.3 kyr. However, the $WAR_{regolith}$ is much faster (334 ± 46 mm kyr^{-1}) than the WAR_{rind}, reflecting faster weathering before the time period recorded by the WAR_{rind}.

The majority of mineral dissolution rates presented within this study are several orders of magnitude faster than field-determined rates previously reported in the literature and some match or are even faster than laboratory determined dissolution rates. This study calculates field-determined mineral dissolution rates only over the weathering front at which they occur (mm-scale in this study) avoiding issues relating to over-scaling (to a m-scale or km-scale), mineral exposure time (ageing of mineral surfaces) and surface area normalization; all of which have previously been suggested to slow mineral dissolution rates. Employing this method minimizes, and in some cases overcomes, the field-laboratory discrepancy in dissolution rates, suggesting that scale is a key factor in calculating mineral dissolution rates.

The mineral grain-scale mechanisms that drive weathering within the Bisley watershed, coupled with the insights gleaned from observing the system with various sized 'rulers' and 'watches', acts to highlight the need for further weathering studies to be conducted on multiple scales (both temporally and spatially), especially on a mineral grain scale, which is only infrequently done. Approaching systems in this manner may solve the field-laboratory discrepancies in mineral dissolution rates by accounting for scaling issues. It would also strengthen the justifications of scaling up weathering rates spatially and also over long time-scales when modeling past, present, and future global carbon cycling.

Acknowledgements

We thank Stuart Kearns (University of Bristol), Tina Geraki (Diamond Light Source) and Lin Ma (University of Texas) for their invaluable advice and guidance. We also thank Manuel Rosario-Torres (USGS) and María Chapela Lara (University of New Hampshire) for field support and Grizelle González (USFS) for help with access. We thank William Nash for providing comparison XANES spectra. We acknowledge funding support from the NSF Luquillo CZO (NSF EAR-0722476 and EAR-1331841), Diamond Light Source (Session SP12005-1) and a PhD fellowship from NERC (for O.W. Moore).

Data Access Statement – all underlying data are provided within this paper or provided as supplementary information accompanying this paper.

References

Ague, J. (1994) Mass transfer during Barrovian metamorphism of pelites, south-central Connecticut; I, Evidence for changes in composition and volume. *Am. J. Sci.,* **294**, 989-1057.

Anderson, S. and Dietrich, W. (2001) Chemical weathering and runoff chemistry in a steep headwater catchment. *Hydrol. Process.,* **15**, 1791-1815.

Anderson, S., Dietrich, W. and Brimhall, G. (2002) Weathering profiles, mass-balance analysis, and rates of solute loss: Linkages between weathering and erosion in a small, steep catchment. *Geol. Soc. Am. Bull.,* **114**, 1143-1158.

Bahlburg, H. and Dobrzinski, N. (2011) A review of the Chemical Index of Alteration (CIA) and its application to the study of Neoproterozoic glacial deposits and climate transitions. *Geol. Soc. Lon. Mem.,* **36**, 81-92.

Balogh-Brunstad, Z., Keller, C.K., Gill, R.A., Bormann, B.T. and Li, C.Y. (2008) The effect of bacteria and fungi on chemical weathering and chemical denudation fluxes in pine growth experiments. *Biogeochem.*, **88**(2), 153-167.

Barth, T. (1961) Abundance of the elements, areal averages and geochemical cycles. *Geochim. Cosmochim. Acta*, **23**, 1-8.

Bazilevskaya, E., Lebedeva, M., Pavich, M., Rother, G., Parkinson, D., Cole, D. and Brantley, S. (2013) Where fast weathering creates thin regolith and slow weathering creates thick regolith. *Earth. Surf. Proc. Land.*, **38**, 847-858.

Bazilevskaya, E., Rother, G., Mildner, D., Pavich, M., Cole, D., Bhatt, M., Jin, L., Steefel, C. and Brantley, S. (2015) How oxidation and dissolution in diabase and granite control porosity during weathering. *Soil. Sci. Soc. Am. J.*, **79**, 55-73.

Behrens, R., Bouchez, J., Schuessler, J., Dultz, S., Hewawasam, T. and von Blanckenburg, F. (2015) Mineralogical transformations set slow weathering rates in low-porosity metamorphic bedrock on mountain slopes in a tropical climate. *Chem. Geol.*, **411**, 283-298.

Benedetti, M., Menard, O., Noack, Y., Carvalho, A. and Nahon, D. (1994) Water-rock interactions in tropical catchments: field rates of weathering and biomass impact. *Chem. Geol.*, **118**, 203-220.

Berner, R., Lasaga, A. and Garrels, R. (1983) The carbonate-silicate geochemical cycle and its effect on atmospheric carbon dioxide over the past 100 million years. *Am. J. Sci.*, **283**, 641-683.

Bierens de Haan, S. (1991) A review of the rate of pyrite oxidation in aqueous systems at low temperature. *Earth-sci. Rev.*, **31**, 1-10.

Bluth, G. and Kump, L. (1994) Lithologic and climatologic controls of river chemistry. *Geochim. Cosmochim. Acta*, **58**, 2341-2359.

Brantley, S. and Chen, Y. (1995) Chemical weathering rates of pyroxenes and amphiboles. *Rev. Min. Geochem.*, **31**, 119-172.

Brantley, S., Holleran, M., Jin, L. and Bazilevskaya, E. (2013) Probing deep weathering in the Shale Hills Critical Zone Observatory, Pennsylvania (USA): the hypothesis of nested chemical reaction fronts in the subsurface. *Earth. Surf. Proc. Land.*, **38**, 1280-1298.

Brantley, S., Lebedeva, M., Balashov, V., Singha, K., Sullivan, P. and Stinchcomb, G. (2017) Toward a conceptual model relating chemical reaction fronts to water flow paths in hills. *Geomorphology*, **277**, 100-117.

Brantley, S., Lebedeva, M. and Bazilevskaya, E. (2014) Relating Weathering Fronts for Acid Neutralization and Oxidation to pCO_2 and pO_2. *Treatise on Geochemistry, Second edition*, Editors: HD Holland, KK Turekian, 327-352.

Briggs, R.P. and Aguilar-Cortés, E. (1980) Geologic Map of Fajardo and Cayo Icacos Quadrangles, Puerto Rico. *USGS Miscellaneous Geological Investigations*, US Geological Survey.

Brimhall, G.H. and Dietrich, W.E. (1987) Constitutive mass balance relations between chemical composition, volume, density, porosity, and strain in metasomatic hydrochemical systems: results on weathering and pedogenesis. *Geochim. Cosmochim. Acta*, **51**, 567-587.

Buss, H., Brantley, S., Scatena, F., Bazilievskaya, E., Blum, A., Schulz, M., Jiménez, R., White, A., Rother, G. and Cole, D. (2013) Probing the deep critical zone beneath the Luquillo Experimental Forest, Puerto Rico. *Earth. Surf. Proc. Land.*, **38**, 1170-1186.

Buss, H., Bruns, M., Schultz, M., Moore, J., Mathur, C. and Brantley, S. (2005) The coupling of biological iron cycling and mineral weathering during saprolite formation, Luquillo Mountains, Puerto Rico. *Geobiology*, **3**, 247-260.

Buss, H., Chapela-Lara, M., Moore, O., Kurtz, A., Schultz, M. and White, A. (2017) Lithological influences on contemporary and long-term regolith weathering at the Luquillo Critical Zone Observatory. *Geochim. Cosmochim. Acta*, **196**, 224-251.

Buss, H., Mathur, R., White, A. and Brantley, S. (2010) Phosphorus and iron cycling in deep saprolite, Luquillo Mountains, Puerto Rico. *Chem. Geol.*, **269**, 52-61.

Buss, H., Sak, P., Webb, S. and Brantley, S. (2008) Weathering of the Rio Blanco quartz diorite, Luquillo Mountains, Puerto Rico: Coupling oxidation, dissolution, and fracturing. *Geochim. Cosmochim. Acta*, **72**, 4488-4507.

Caldeira, C., Ciminelli, V. and Osseo-Asare, K. (2010) The role of carbonate ions in pyrite oxidation in aqueous systems. *Geochim. Cosmochim. Acta*, **74**, 1777-1789.

Carretier, S., Goddéris, Y., Delannoy, T. and Rouby, D. (2014) Mean bedrock-to-saprolite conversion and erosion rates during mountain growth and decline. *Geomorphology*, **209**, 39-52.

Chabaux, F., Blaes, E., Stille, P., di Chiara Roupert, R., Pelt, E., Dosseto, A., Ma, L., Buss, H. and Brantley, S. (2013) Regolith formation rate from U-series nuclides: implications from the study of a spheroidal weathering profile in the Rio Icacos watershed (Puerto Rico). *Geochim. Cosmochim. Acta*, **100**, 73-95.

Chabaux, F., Bourdon, B. and Riotte, J. (2008) U-series geochemistry in weathering profiles, river waters and lakes. U/Th Series Radionuclides in Aquatic Systems. *Radioact. Environ.*, **13**, 49-104.

Chabaux, F., Ma, L., Stille, P., Pelt, E., Granet, M., Lemarchand, D., di Chiara Roupert, R. and Brantley, S. (2011) Determination of chemical weathering rates from U series nuclides in soils and weathering profiles: Principles, applications and limitations. *Appl. Geochem.*, **26**, S20-S23.

Chabaux, F., Riotte, J. and Dequincey, O. (2003) U-Th-Ra fractionation during weathering and river transport. *Rev. Min. Geochem.*, **52**, 533-576.

Chapela Lara, M., Buss, H., Pogge von Strandmann, P., Schuessler, J. and Moore, O. (2017) The influence of critical zone processes on the Mg isotope budget in a tropical, highly weathered andesitic catchment. *Geochim. Cosmochim. Acta.*, **202**, 77-100.

Choppala, G., Bush, R., Moon, E., Ward, N., Wang, Z., Bolan, N. and Sullivan, L. (2017) Oxidative transformation of iron monosulfides and pyrite in estuarine sediments: Implications for trace metals mobilisation. *J. Environ. Manage.*, **186**, 158-166.

Czapla, J., Kwiatek, W., Lekki, J., Steininger, R. and Gottlicher, J. (2012) Determination of Changes in Sulphur Oxidation States in Prostate Cancer Cells. *Acta. Phys. Pol. A*, **121**, 497-501.

Dellinger, M., Bouchez, J., Gaillardet, J. and Faure, L. (2015) Testing the Steady State Assumption for the Earth's Surface Denudation Using Li Isotopes in the Amazon Basin. *Proc. Earth. Plan. Sci.*, **13**, 162-168.

Dequincey, O., Chabaux, F., Clauer, N., Liewig, N. and Muller, J. (1999) Dating of weathering profiles by radioactive disequilibria: contribution of the study of authigenic mineral fractions. *Comptes Rendus de l'Académie des Sciences-Series IIA – Earth. Plan. Sci.*, **328**, 679-685.

Dequincey, O., Chabaux, F., Clauer, N., Sigmarsson, O., Liewig, N. and Leprun, J.-C. (2002) Chemical mobilizations in laterites: evidence from trace elements and ^{238}U-^{234}U-^{230}Th disequilibria. *Geochim. Cosmochim. Acta*, **66**, 1197-1210.

Dessert, C., Dupré, B., Gaillardet, J., François, L. and Allegre, C. (2003) Basalt weathering laws and the impact of basalt weathering on the global carbon cycle. *Chem. Geol.*, **202**, 257-273.

Dosseto, A., Buss, H. and Chabaux, F. (2014) Age and weathering rate of sediments in small catchments: the role of hillslope erosion. *Geochim. Cosmochim. Acta*, **132**, 238-258.

Dosseto, A., Buss, H. and Suresh, P. (2012) Rapid regolith formation over volcanic bedrock and implications for landscape evolution. *Earth Planet. Sci. Lett.*, **337**, 47-55.

Dosseto, A., Turner, S. and Chappell, J. (2008) The evolution of weathering profiles through time: New insights from uranium-series isotopes. *Earth Planet. Sci. Lett.*, **274**, 359-371.

Drever, J. and Stillings, L. (1997) The role of organic acids in mineral weathering. *Colloids Surf. A: Physicochemical and Engineering Aspects*, **120**, 167-181.

Eggler, D., Larson, E. and Bradley, W. (1969) Granites, grusses, and the Sherman erosion surface, southern Laramie Range, Colorado-Wyoming. *Am. J. Sci.*, **267**, 510-522.

España, J., Pamo, E. and Pastor, E. (2007) The oxidation of ferrous iron in acidic mine effluents from the Iberian Pyrite Belt (Odiel Basin, Huelva, Spain): field and laboratory rates. *J. Geochem. Explor.*, **92**, 120-132.

Etienne, S. (2002) The role of biological weathering in periglacial areas: a study of weathering rinds in south Iceland. *Geomorphology*, **47**, 75-86.

Fedo, C., Nesbitt, H. and Young, G. (1995) Unraveling the effects of potassium metasomatism in sedimentary rocks and paleosols, with implications for paleoweathering conditions and provenance. *Geology*, **23**, 921-924.

Field, J., Breshears, D.D., Law, D., Villegas, J., López-Hoffman, L., Brooks, P., Chorover, J., Barron-Gafford, G., Gallery, R. and Litvak, M. (2015) Critical Zone services: Expanding context, constraints, and currency beyond ecosystem services. *V. Z. J.*, **14** (1).

Fleet, M., Liu, X., Harmer, S. and Nesbitt, W. (2005) Chemical state of sulfur in natural and synthetic lazurite by S K-edge XANES and X-ray photoelectron spectroscopy. *Can. Mineral.*, **43**, 1589-1603.

Fletcher, R., Buss, H. and Brantley, S. (2006) A spheroidal weathering model coupling porewater chemistry to soil thicknesses during steady-state denudation. *Earth Planet. Sci. Lett.*, **244**, 444-457.

Gaillardet, J., Dupré, B., Louvat, P. and Allegre, C. (1999) Global silicate weathering and CO_2 consumption rates deduced from the chemistry of large rivers. *Chem. Geol.*, **159**, 3-30.

Gaillardet, J., Rad, S., Rivé, K., Louvat, P., Gorge, C., Allègre, C. and Lajeunesse, E. (2011) Orography-driven chemical denudation in the Lesser Antilles: Evidence for a new feed-back mechanism stabilizing atmospheric CO_2. *Am. J. Sci.*, **311**, 851-894.

Garcia-Martino, A.R., Warner, G.S., Scatena, F.N. and Civco, D.L. (1996) Rainfall, runoff and elevation relationships in the Luquillo Mountains of Puerto Rico. *Caribb. J. Sci.*, **32**, 413-424.

Gardner, L. (1980) Mobilization of Al and Ti during weathering—isovolumetric geochemical evidence. *Chem. Geol.*, **30**, 151-165.

Gartman, A. and Luther, G. (2014) Oxidation of synthesized sub-micron pyrite (FeS_2) in seawater. *Geochim. Cosmochim. Acta*, **144**, 96-108.

Gautier, J.M., Oelkers, E. and Schott, J. (2001) Are quartz dissolution rates proportional to BET surface areas? *Geochim. Cosmochim. Acta*, **65**, 1059-1070.

Ghaleb, B., Hillaire-Marcel, C., Causse, C., Gariepy, C. and Vallieres, S. (1990) Fractionation and recycling of U and Th isotopes in a semi-arid endoreic depression of central Syria. *Geochim. Cosmochim. Acta*, **54**, 1025-1035.

Goldsmith, S., Carey, A., Johnson, B., Welch, S., Lyons, W., McDowell, W. and Pigott, J. (2010) Stream geochemistry, chemical weathering and CO_2 consumption potential of andesitic terrains, Dominica, Lesser Antilles. *Geochim. Cosmochim. Acta*, **74**, 85-103.

Gonzalez, G. (2011) Data a product of USDA Forest Service -IITF: http://luq.lternet.edu/data Under grants BSR-8811902, DEB 9411973, DEB 0080538, DEB 0218039, DEB 0620910, DEB 0963447 AND DEB-129764 from NSF to the Department of Environmental Science, University of Puerto Rico, and to the International Institute of Tropical Forestry USDA Forest Service, as part of the Luquillo Long-Term Ecological Research Program.

Goodfellow, B., Hilley, G., Webb, S., Sklar, L.S., Moon, S. and Olson, C. (2016) The chemical, mechanical, and hydrological evolution of weathering granitoid. *J. Geophys. Res. Earth Surf.*, **121**, 1410-1435.

Graham, R., Rossi, A. and Hubbert, K. (2010) Rock to regolith conversion: Producing hospitable substrates for terrestrial ecosystems. *GSA Today*, **20**, 4-9.

Gustafsson, Å. and Puigdomenech, I. (2003) The effect of pH on chlorite dissolution rates at 25 °C. *Scientific Basis for Nuclear Waste Management XXVI*, **757**, 649-655.

Hamilton, J., Pantano, C. and Brantley, S. (2000) Dissolution of albite glass and crystal. *Geochim. Cosmochim. Acta*, **64**, 2603-2615.

Hansen, R. and Stout, P.R. (1968) Isotopic distributions of uranium and thorium in soils. *Soil Sci.*, **105**, 44-50.

Heartsill-Scalley, T., Scatena, F.N., Estrada, C., McDowell, W. and Lugo, A.E. (2007) Disturbance and long-term patterns of rainfall and throughfall nutrient fluxes in a subtropical wet forest in Puerto Rico. *J. Hydrol.*, **333**, 472-485.

Heidari, P., Li, L., Jin, L., Williams, J. and Brantley, S. (2017) A Reactive Transport Model for Marcellus Shale Weathering. *Geochim. Cosmochim. Acta*, **217**, 421-440.

Heimsath, A., Dietrich, W., Nishiizumi, K. and Finkel, R. (1997) The soil production function and landscape equilibrium. *Nature*, **388**, 358-361.

Helgeson, H., Murphy, W. and Aagaard, P. (1984) Thermodynamic and kinetic constraints on reaction rates among minerals and aqueous solutions. II. Rate constants, effective surface area, and the hydrolysis of feldspar. *Geochim. Cosmochim. Acta*, **48**, 2405-2432.

Herrera, R., Jordan, C., Klinge, H. and Medina, E. (1978a) Amazon ecosystems. Their structure and functioning with particular emphasis on nutrients. *Interciencia*, **3**, 223-231.

Herrera, R., Merida, T., Stark, N. and Jordan, C. (1978b) Direct phosphorus transfer from leaf litter to roots. *Naturwissenschaften*, **65**, 208-209.

Hodell, DA and Curtis, JH (1991) Reconstruction of Caribbean climate change over the past 10,500 years. *Nature*, **352**, 790.

Holbrook, W., Riebe, C., Elwaseif, M., Hayes, J., Basler-Reeder, K., Harry, D., Malazian, A., Dosseto, A., Hartsough, P. and Hopmans, J. (2014) Geophysical constraints on deep weathering and water storage potential in the Southern Sierra Critical Zone Observatory. *Earth Surf. Process. and Landf.*, **39**, 366-380.

Hynek, S., Comas, X. and Brantley, S. (2017) The Effect of Fractures on Weathering of Igneous and Volcaniclastic Sedimentary Rocks in the Puerto Rican Tropical Rain Forest. *Proc. Earth. Plan. Sci.*, **17**, 972-975.

Jamtveit, B., Kobchenko, M., Austrheim, H., Malthe-Sørenssen, A., Røyne, A. and Svensen, H. (2011) Porosity evolution and crystallization-driven fragmentation during weathering of andesite. *J. Geophys. Res.*, **116**, B12204.

Jolly, W.T., Lidiak, E.G., Schellekens, J.H. and Santos, H. (1998) Volcanism, tectonics, and stratigraphic correlations in Puerto Rico. *Geol. Soc. Spec. Pap.*, **322**, 1-34.

Kalinowski, B., Faith-Ell, C. and Schweda, P. (1998) Dissolution kinetics and alteration of epidote in acidic solutions at 25 ^{o}C. *Chem. Geol.*, **151**, 181-197.

Knauss, K. and Wolery, T. (1986) Dependence of albite dissolution kinetics on pH and time at 25 ^{o}C and 70 ^{o}C. *Geochim. Cosmochim. Acta*, **50**, 2481-2497.

Kurtz, A.C., Lugolobi, F. and Salvucci, G. (2011) Germanium-silicon as a flow path tracer: Application to the Rio Icacos watershed. *Water Resour. Res.*, **47**, W06516.

Lawrence, C., Harden, J. and Maher, K. (2014) Modeling the influence of organic acids on soil weathering. *Geochim. Cosmochim. Acta*, **139**, 487-507.

Lebedeva, M. and Brantley, S. (2013) Exploring geochemical controls on weathering and erosion of convex hillslopes: beyond the empirical regolith production function. *Earth Surf. Process. Landf.*, **38**, 1793-1807.

Lichtner, P. (1988) The quasi-stationary state approximation to coupled mass transport and fluid-rock interaction in a porous medium. *Geochim. Cosmochim. Acta*, **52**, 143-165.

Liptzin, D., Silver, W. and Detto, M. (2011) Temporal dynamics in soil oxygen and greenhouse gases in two humid tropical forests. *Ecosystems*, **14**, 171-182.

Lowson, R. (1982) Aqueous oxidation of pyrite by molecular oxygen. *Chem. Rev.*, **82**, 461-497.

Lowson, R., Brown, P., Comarmond, M.C.J. and Rajaratnam, G. (2007) The kinetics of chlorite dissolution. *Geochim. Cosmochim. Acta*, **71**, 1431-1447.

Luo, X., Rehkämper, M., Lee, D.-C. and Halliday, A. (1997) High precision $^{230}Th/^{232}Th$ and $^{234}U/^{238}U$ measurements using energy filtered ICP magnetic sector multiple collector mass spectrometry. *Int. J. Mass Spectrom. Ion Process.*, **171**, 105-117.

Ma, L., Chabaux, F., Pelt, E., Blaes, E., Jin, L. and Brantley, S. (2010) Regolith production rates calculated with uranium-series isotopes at Susquehanna/Shale Hills Critical Zone Observatory. *Earth Planet. Sci. Lett.*, **297**, 211-225.

Ma, L., Chabaux, F., Pelt, E., Granet, M., Sak, P., Gaillardet, J., Lebedeva, M. and Brantley, S. (2012) The effect of curvature on weathering rind formation: Evidence from Uranium-series isotopes in basaltic andesite weathering clasts in Guadeloupe. *Geochim. Cosmochim. Acta*, **80**, 92-107.

Ma, L., Chabaux, F., West, N., Kirby, E., Jin, L. and Brantley, S. (2013) Regolith production and transport in the Susquehanna Shale Hills Critical Zone Observatory, Part 1: Insights from U-series isotopes. *J. Geophys. Res. Earth Surf.*, **118**, 722-740.

Ma, L., Jin, L. and Brantley, S. (2011) How mineralogy and slope aspect affect REE release and fractionation during shale weathering in the Susquehanna/Shale Hills Critical Zone Observatory. *Chem. Geol.*, **290**, 31-49.

Maher, K. (2010) The dependence of chemical weathering rates on fluid residence time. *Earth Planet. Sci. Lett.*, **294**, 101-110.

Malmström, M.E., Destouni, G., Banwart, S.A. and Strömberg, B.H. (2000) Resolving the scale-dependence of mineral weathering rates. *Environ. Sci. Technol.*, **34**(7), pp.1375-1378.

Mayewski, PA, Rohling, EE, Stager, J C, Karlén, W, Maasch, KA, Meeker, L D, Meyerson, EA, Gasse, F, van Kreveld, S and Holmgren, K (2004) Holocene climate variability. *Quat. Res.*, **62**, 243-255.

McDowell, W. (1998) Internal nutrient fluxes in a Puerto Rican rain forest. *J. Trop. Ecol.*, **14**, 521-536.

McDowell, W. (2001) Hurricanes, people, and riparian zones: controls on nutrient losses from forested Caribbean watersheds. *Forest Ecol. Manag.*, **154**, 443-451.

McDowell, W. (2010) Chemistry of stream water from the Luquillo Mountains. Long Term Ecological Research Network. http://dx.doi.org/10.6073/pasta/63e41fb1bb1bf05d7cdca90c55769fa4.

McDowell, W. (2012) Chemistry of rainfall and throughfall from El Verde and Bisley. Long Term Ecological Research Network. http://dx.doi.org/10.6073/pasta/d113d7ac3a23d3a9cbdc0824789640e7.

McKean, J., Dietrich, W., Finkel, R., Southon, J. and Caffee, M. (1993) Quantification of soil production and downslope creep rates from cosmogenic ^{10}Be accumulations on a hillslope profile. *Geology*, **21**, 343-346.

McKibben, M. and Barnes, H. (1986) Oxidation of pyrite in low temperature acidic solutions: Rate laws and surface textures. *Geochim. Cosmochim. Acta*, **50**, 1509-1520.

McTainsh, G. (1980) Harmattan dust deposition in northern Nigeria. *Nature*, **286**, 587-588.

Mellott, N., Brantley, S. and Pantano, C. (2002) Topography of polished plates of albite crystal and glass during dissolution. Water-Rock Interactions, Ore Deposits, and Environmental Geochemistry: A Tribute to David A. Crerar. *Geochem. Soc. Spec. Pub.*, **7**, 83-95.

Métrich, N., Berry, A., O'Neill, H.S.C. and Susini, J. (2009) The oxidation state of sulfur in synthetic and natural glasses determined by X-ray absorption spectroscopy. *Geochim. Cosmochim. Acta*, **73**, 2382-2399.

Meybeck, M. (1987) Global chemical weathering of surficial rocks estimated from river dissolved loads. *Am. J. Sci.*, **287**, 401-428.

Mironenko, M. and Cherkasova, E. (2017) Thermodynamic-kinetic Modeling of Chemical Weathering of Basaltic Tephra on Hawaii. *Proc. Earth. Plan. Sci.*, **17**, 124-127.

Nagarajan, R., Roy, P., Jonathan, M., Lozano, R., Kessler, F. and Prasanna, M. (2014) Geochemistry of Neogene sedimentary rocks from Borneo Basin, East Malaysia: Paleo-weathering, provenance and tectonic setting. *Chem. Erde*, **74**, 139-146.

Navarre-Sitchler, A. and Brantley, S. (2007) Basalt weathering across scales. *Earth Planet. Sci. Lett.*, **261**, 321-334.

Navarre-Sitchler, A., Cole, D., Rother, G., Jin, L., Buss, H. and Brantley, S. (2013) Porosity and surface area evolution during weathering of two igneous rocks. *Geochim. Cosmochim. Acta*, **109**, 400-413.

Navarre-Sitchler, A., Steefel, C., Sak, P. and Brantley, S. (2011) A reactive-transport model for weathering rind formation on basalt. *Geochim. Cosmochim. Acta*, **75**, 7644-7667.

Navarre-Sitchler, A., Steefel, C., Yang, L., Tomutsa, L. and Brantley, S. (2009) Evolution of porosity and diffusivity associated with chemical weathering of a basalt clast. *J. Geophys. Res. Earth Surf.*, **114**, F02016

Nesbitt, I. and Young, G. (1982) Early Proterozoic climates and plate. *Nature*, **299**, 21.

Nicholson, R. (1994) Iron-sulfide oxidation mechanisms: laboratory studies. In: Jambor J.L. and D.W. Blowes, eds. Environmental Geochemistry of Sulfide Mine-Wates. *Mineralogical Society of America*, 163-183.

Nugent, M., Brantley, S., Pantano, C. and Maurice, P. (1998) The influence of natural mineral coatings on feldspar weathering. *Nature*, **395**, 588.

Palandri, J.L. and Kharaka, Y.K. (2004) A compilation of rate parameters of water-mineral interaction kinetics for application to geochemical modeling (No. OPEN-FILE-2004-1068). Geological Survey Menlo Park CA.

Pavich, M., Brown, L., Valette-Silver, J., Klein, J. and Middleton, R. (1985) ^{10}Be analysis of a Quaternary weathering profile in the Virginia Piedmont. *Geology*, **13**, 39-41.

Peacock, Caroline & Moon, Ellen. (2012). Oxidative scavenging of thallium by birnessite: Explanation for thallium enrichment and stable isotope fractionation in marine ferromanganese precipitates. *Geochim. Cosmochim. Acta*, **84**, 297–313.

Pelt, E., Chabaux, F., Innocent, C., Navarre-Sitchler, A.K., Sak, P. and Brantley, S.L. (2008) Uranium–thorium chronometry of weathering rinds: rock alteration rate and paleo-isotopic record of weathering fluids. *Earth Planet. Sci. Lett.*, **276**, 98-105.

Pett-Ridge, J. (2009) Contributions of dust to phosphorus cycling in tropical forests of the Luquillo Mountains, Puerto Rico. *Biogeochemistry*, **94**, 63-80.

Price, J.R., Heitmann, N., Hull, J. and Szymanski, D. (2008) Long-term average mineral weathering rates from watershed geochemical mass balance methods: Using mineral modal abundances to solve more equations in more unknowns. Chemical Geology, **254**, 36-51.

Rad, S., Allègre, C. and Louvat, P. (2007) Hidden erosion on volcanic islands. *Earth Planet. Sci. Lett.*, **262**, 109-124.

Rempe, D. and Dietrich, W. (2014) A bottom-up control on fresh-bedrock topography under landscapes. *Proc. Natl. Acad. Sci. U. S. A.*, **111**, 6576-6581.

Richter, D. and Markewitz, D. (1995) How deep is soil? *BioScience*, **45**, 600-609.

Riebe, C., Hahm, W. and Brantley, S. (2017) Controls on deep critical zone architecture: a historical review and four testable hypotheses. *Earth Surf. Process. Landf.*, **42**, 128-156.

Riebe, C., Kirchner, J. and Finkel, R. (2004) Erosional and climatic effects on long-term chemical weathering rates in granitic landscapes spanning diverse climate regimes. *Earth Planet. Sci. Lett.*, **224**, 547-562.

Rose, N.M. (1991) Dissolution rates of prehnite, epidote, and albite. *Geochim. Cosmochim. Acta*, **55,** 3273-3286.

Rosholt, J., Doe, B. and Tatsumoto, M. (1966) Evolution of the isotopic composition of uranium and thorium in soil profiles. *Geol. Soc. Am. Bull.*, **77**, 987-1004.

Sak, P., Fisher, D., Gardner, T., Murphy, K. and Brantley, S. (2004) Rates of weathering rind formation on Costa Rican basalt. *Geochim. Cosmochim. Acta*, **68**, 1453-1472.

1594 Sak, P., Navarre-Sitchler, A., Miller, C., Daniel, C., Gaillardet, J., Buss, H., Lebedeva, M.
1595 and Brantley, S. (2010) Controls on rind thickness on basaltic andesite clasts
1596 weathering in Guadeloupe. Chem. Geol., **276**, 129-143.
1597
1598 Scatena, F.N. (1989) An introduction to the physiography and history of the Bisley
1599 Experimental Watersheds in the Luquillo Mountains of Puerto Rico. Gen. Tech. Rep.
1600 SO-72. New Orleans, LA: US Dept of Agriculture, Forest Service, Southern Forest
1601 Experiment Station, 22.
1602
1603 Schellekens, J., Scatena, F., Bruijnzeel, L., Van Dijk, A., Groen, M. and Van Hogezand, R.
1604 (2004) Stormflow generation in a small rainforest catchment in the Luquillo
1605 Experimental Forest, Puerto Rico. *Hydrol. Process.*, **18**, 505-530.
1606
1607 Schopka, H. and Derry, L. (2012) Chemical weathering fluxes from volcanic islands and the
1608 importance of groundwater: The Hawaiian example. *Earth Planet. Sci. Lett.*, **339**, 67-
1609 78.
1610
1611 Schulz, M. and White, A. (1999) Chemical weathering in a tropical watershed, Luquillo
1612 Mountains, Puerto Rico III: quartz dissolution rates. *Geochim. Cosmochim. Acta*, **63**,
1613 337-350.
1614
1615 Sheng, Z. and Kuroda, P. (1986) Isotopic fractionation of uranium: Extremely high
1616 enrichments of ^{234}U in the acid-residues of a Colorado carnotite. *Radiochim. Acta*, **39**,
1617 131-138.
1618
1619 Sims, K., Gill, J., Dosseto, A., Hoffmann, D., Lundstrom, C., Williams, R., Ball, L.,
1620 Tollstrup, D., Turner, S. and Prytulak, J. (2008) An inter-laboratory assessment of the
1621 thorium isotopic composition of synthetic and rock reference materials. *Geostand.*
1622 *Geoanal. Res.*, **32**, 65-91.
1623
1624 Smith, A.L., Schellekens, J.H. and Díaz, A.-L.M. (1998) Batholiths as markers of tectonic
1625 change in the northeastern Caribbean. *Spec. Pap. Geol. Soc. Am.*, 99-122.
1626
1627 St. Clair, J., Moon, S., Holbrook, W., Perron, J., Riebe, C., Martel, S., Carr, B., Harman, C.
1628 and Singha, K. (2015) Geophysical imaging reveals topographic stress control of
1629 bedrock weathering. *Science*, **350**, 534-538.
1630
1631 Stallard, R. and Edmond, J. (1983) Geochemistry of the Amazon: 2. The influence of geology
1632 and weathering environment on the dissolved load. *J. Geophys. Res. Oceans*, **88**,
1633 9671-9688.
1634
1635 Stark, N. and Jordan, C. (1978) Nutrient retention by the root mat of an Amazonian rain
1636 forest. *Ecology*, **59**, 434-437.
1637
1638 Stoorvogel, J., Van Breemen, N. and Jassen, B. (1997) The nutrient input by Harmattan dust
1639 to a forest ecosystem in Cote d'Ivoire, Africa. *Biogeochem.*, **37**, 145-157.
1640
1641 Stretch, R. and Viles, H. (2002) The nature and rate of weathering by lichens on lava flows
1642 on Lanzarote. *Geomorphology*, **47**, 87-94.

Sverdrup, H. (1990) The kinetics of base cation release due to chemical weathering. Lund University Press, ISBN: 9789179661090

Taylor, R. and McKenzie, R. (1966) The association of trace elements with manganese minerals in Australian soils. *Soil Research*, **4**, 29-39.

Tipper, E., Bickle, M., Galy, A., West, A., Pomiès, C. and Chapman, H. (2006) The short term climatic sensitivity of carbonate and silicate weathering fluxes: insight from seasonal variations in river chemistry. *Geochim. Cosmochim. Acta*, **70**, 2737-2754.

Turner, B., Stallard, R. and Brantley, S. (2003) Investigation of in situ weathering of quartz diorite bedrock in the Rio Icacos basin, Luquillo Experimental Forest, Puerto Rico. *Chem. Geol.*, **202**, 313-341.

van Haren, J., Dontsova, K., Barron-Gafford, G., Troch, P., Chorover, J., Delong, S., Breshears, D., Huxman, T., Pelletier, J. and Saleska, S. (2017) CO_2 diffusion into pore spaces limits weathering rate of an experimental basalt landscape. *Geology*, **45** (3), 203-206.

Von Blanckenburg, F. (2005) The control mechanisms of erosion and weathering at basin scale from cosmogenic nuclides in river sediment. *Earth Planet. Sci. Lett.*, **237**, 462-479.

Vuorinen, A. and Carlson, L. (1985) Scavenging of heavy metals by hydrous Fe and Mn oxides precipitating from ground water in Finland, *Proc. Int. Conf. Heavy Metals Environ. Athens I*, 266-268.

Walker, J., Hays, P. and Kasting, J. (1981) A negative feedback mechanism for the long-term stabilization of Earth's surface temperature. *J. Geophys. Res. Oceans*, **86**, 9776-9782.

West, A., Galy, A. and Bickle, M. (2005) Tectonic and climatic controls on silicate weathering. *Earth Planet. Sci. Lett.*, **235**, 211-228.

White, A. (2002) Determining mineral weathering rates based on solid and solute weathering gradients and velocities: application to biotite weathering in saprolites. *Chem. Geol.*, **190**, 69-89.

White, A. and Blum, A. (1995) Effects of climate on chemical weathering in watersheds. *Geochim. Cosmochim. Acta*, **59**, 1729-1747.

White, A., Blum, A., Schulz, M., Bullen, T., Harden, J. and Peterson, M. (1996) Chemical weathering rates of a soil chronosequence on granitic alluvium: I. Quantification of mineralogical and surface area changes and calculation of primary silicate reaction rates. *Geochim. Cosmochim. Acta*, **60**, 2533-2550.

White, A., Blum, A., Schulz, M., Vivit, D., Stonestrom, D., Larsen, M., Murphy, S. and Eberl, D. (1998) Chemical weathering in a tropical watershed, Luquillo Mountains, Puerto Rico: I. Long-term versus short-term weathering fluxes. *Geochim. Cosmochim. Acta*, **62**, 209-226.

White, A. and Brantley, S. (2003) The effect of time on the weathering of silicate minerals: why do weathering rates differ in the laboratory and field? *Chem. Geol.*, **202**, 479-506.

White, A., Bullen, T., Schulz, M., Blum, A., Huntington, T. and Peters, N. (2001) Differential rates of feldspar weathering in granitic regoliths. *Geochim. Cosmochim. Acta*, **65**, 847-869.

White, A. and Peterson, M. (1990) The role of reactive surface areas in chemical weathering. *Chem. Geol.*, **84**, 334-336.

White, A., Schulz, M., Lowenstern, J., Vivit, D. and Bullen, T. (2005) The ubiquitous nature of accessory calcite in granitoid rocks: implications for weathering, solute evolution, and petrogenesis. *Geochim. Cosmochim. Acta*, **69**, 1455-1471.

Wong, J., Lytle, F., Messmer, R. and Maylotte, D. (1984) K-edge absorption spectra of selected vanadium compounds. *Phys. Rev. B*, **30**, 5596.

Zhu, C., Blum, A. and Veblen, D. (2004) Feldspar dissolution rates and clay precipitation in the Navajo aquifer at Black Mesa, Arizona, USA. Water-Rock Interaction, 895-899.

Table 1. Mineralogy of unweathered bedrock and mineralogy of weathered rind in B1W1 sample.

Mineral	Abundance of mineral in parent rock[a]	Diameter of mineral (D)[b]	Abundance of mineral in weathered rind[a]	Mineral specific density (ρ_m)	Mineral Formula[c]
	vol%	µm	vol%	(g cm^{-3})	
Albite	35.2 ± 0.7	126 ± 15	11.8 ± 0.7	2.6[e]	$(Na_{0.94},Ca_{0.02},Fe^{2+}_{0.01},Mg_{0.01})[Si_{2.96}Al_{1.01}O_{7.97}]$
Chlorite	17.2 ± 0.7	14[d]	12 ± 1	3.0[e]	$(Mg_{4.59},Ca_{0.57},Mn_{0.05},Fe^{2+}_{3.47},Fe^{3+}_{0.32},Al_{2.61})[(Si_{5.95},Al_{2.05})O_{20}]OH_{16}$
Epidote	14 ± 2	31 ± 4	4.7 ± 0.7	3.4[e]	$Ca_{2.11}Fe^{3+}_{0.87}Al_{2.23}Si_{3.11}O_{12}(OH)$
Quartz	11.0 ± 0.9	3 ± 1	11 ± 1	2.7[e]	SiO_2
Pyroxene	7 ± 1	74 ± 8	0.0 ± 0.3	3.4[e]	$(Fe^{2+}_{0.03},Mg_{0.17},Ca_{0.78},Na_{0.02})(Ti_{0.01},Al_{0.04},Fe^{3+}_{0.07},Fe^{2+}_{0.14},Mg_{0.74})(Si_{1.89},Al_{0.11})O_6$
Illite	5 ± 2		0.9 ± 0.7	2.8[e]	
Anorthite	4.4 ± 0.7		0.0 ± 0.0	2.8[e]	
Sphene	2.6 ± 0.9		3.1 ± 0.6	3.5[e]	
Pyrite	0.5 ± 0.2	14 ± 2	0.0 ± 0.0	5.0[e]	FeS_2
Porosity	0.9 ± 0.7		22 ± 3	0.0	
Kaolinite	0.4 ± 0.4		20 ± 2	2.7[e]	
Apatite	0.4 ± 0.2		0.0 ± 0.0	3.3[e]	
Mn-oxide	n.d.[g]		1.4 ± 0.8	3.0[f]	
Fe(III)-(hydr)oxide	< 0.1		11 ± 1	4.3[e]	
Gibbsite	< 0.2		3 ± 1	2.4[e]	

[a]Determined using X-ray phase analysis as described in Section 2.3. Uncertainties represent 1SE (n= 5).
[b]Determined by point counting as described in Section 2.3. Uncertainties represent 1SE (n= 50).
[c]Determined from microprobe analysis.
[d]Buss et al. (2017)
[e]Deer et al. (1997)
[f]Anthony (1997)
[g] not detected

Table 2. Uranium-series measurements[a].

Distance from fracture surface (mm)	Th (ppm)	U (ppm)	U/Th	($^{234}U/^{238}U$)	($^{230}Th/^{238}U$)
1.5	2.27 ± 0.00	1.4 ± 0.00	0.617	1.027 ± 0.001	1.069 ± 0.003
4.5	1.51 ± 0.00	0.98 ± 0.00	0.649	1.014 ± 0.001	0.985 ± 0.003
7.5	1.43 ± 0.00	0.9 ± 0.00	0.629	1.023 ± 0.001	0.999 ± 0.003
10.5	2.1 ± 0.01	0.94 ± 0.00	0.448	1.011 ± 0.001	1.097 ± 0.008
13.5	1.73 ± 0.00	0.93 ± 0.00	0.538	1.016 ± 0.001	1.02 ± 0.003
16.5	1.39 ± 0.01	0.91 ± 0.00	0.655	1.016 ± 0.001	0.994 ± 0.007
19.5	1.41 ± 0.01	0.88 ± 0.00	0.624	1.012 ± 0.001	1.018 ± 0.01
22.5	1.42 ± 0.01	0.88 ± 0.00	0.620	1.012 ± 0.001	1.02 ± 0.019
36.5	1.32 ± 0.02	0.83 ± 0.00	0.629	1.019 ± 0.002	1.001 ± 0.029
46.5	1.26 ± 0.02	0.83 ± 0.00	0.659	1.021 ± 0.001	1.008 ± 0.033
QLO-1				1.006 ± 0.001	1.005 ± 0.004

[a]Errors for samples and rock standard QLO-1 are internal analytical uncertainties given at the 2SE level.

Table 3. Results of nuclide loss-gain model.

Number of samples	10
Initial Conditions	Secular equilibrium
Parameter calculated values[a]	
k_{238} (yr^{-1})	$2.39 \times 10^{-5} \pm 1.1 \times 10^{-6}$
k_{234}/k_{238}	0.88 ± 0.02
k_{230}/k_{238}	$6.12 \times 10^{-5} + 9 \times 10^{-6} / - 8 \times 10^{-6}$
f_{234}/f_{238}	0.80 ± 0.03
Distance from fracture surface	**Weathering age (yr)**[b]
1.5 mm	3190 ± 220
4.5 mm	106 ± 16
7.5 mm	379 ± 43
10.5 mm	4210 ± 270
13.5 mm	1184 ± 103
16.5 mm	160 ± 20
19.5 mm	1082 ± 96
22.5 mm	1163 ± 102
36.5 mm	436 ± 48
46.5 mm	728 ± 72

[a]Uncertainty is presented as 2SE (n = 1000);
[b]Uncertainty is presented as 1SE (n = 1000);

Table 4. Variables and results of mineral specific solid-state dissolution rate equation for B1W1.

Mineral	Mass fraction of mineral in parent material (φ)[a]	Specific surface area (s)[b]	Weathering Gradient (bs)[c]	r_m[d]		Log r_m
	($g\ g^{-1}$)	($m^2\ g^{-1}$)	($m\ kg\ mol^{-1}$)	($mol\ m^{-2}\ s^{-1}$)		
Albite	0.31 ± 0.03	0.1	0.026 ± 0.012	1.1×10^{-12}	$\pm 2.9 \times 10^{-14}$	-12.0
Chlorite	0.17 ± 0.01	1.0	0.222 ± 0.066	2.9×10^{-14}	$\pm 3.8 \times 10^{-16}$	-13.5
Chlorite[e]	0.17 ± 0.01	1.0	0.642 ± 0.008	1.0×10^{-14}	$\pm 1.3 \times 10^{-16}$	-14.0
Epidote	0.18 ± 0.03	0.4	0.040 ± 0.004	4.3×10^{-13}	$\pm 1.4 \times 10^{-15}$	-12.4
Pyroxene	0.08 ± 0.01	0.2	0.057 ± 0.012	1.5×10^{-12}	$\pm 4.8 \times 10^{-15}$	-11.8
Pyroxene[e]	0.08 ± 0.01	0.2	0.120 ± 0.041	6.9×10^{-13}	$\pm 2.3 \times 10^{-15}$	-12.2
Pyrite	0.01 ± 0.00	14	0.123 ± 0.009	1.8×10^{-12}	$\pm 2.4 \times 10^{-15}$	-11.8

[a] Mass fractions were determined from mineral abundances and densities (Table 1). Errors are 1SE.
[b] Calculated using Eq. 6 and mineral data from Table 1.
[c] Weathering gradients were determined from the slope of the normalized concentration plots (Fig. 10). The uncertainty of the weathering gradient is calculated as the maximum and minimum slope gradient from the standard error.
[d] r_m was calculated using Eq. 5, the data in this table and Table 1. Errors are 1SE and propagated fully through all calculations.
[e] Mineral dissolution in association with pyrite.

Figure captions

Fig. 1. Map of field site, including key lithological units within the Luquillo Critical Zone Observatory (LCZO). Dots represent sample locations. B1W1: Bedrock fracture samples (this study); Stream gage: Stream chemistry data (McDowell, 2010; 2012); B1R: Regolith samples (Dosseto et al., 2012).

Fig. 2. Back scattered electron (BSE) images of bedrock thin sections. A) X-ray phase map, false color image showing sericitization of albite (Alb) with illite (ILL, in red). Chl = chlorite, Epi = epidote. B) Mn-oxide precipitation in pore space. C) Kaolinite precipitation in pore space. D) Pitting of albite grain, darker grey areas are depleted in Na. E) Pyrite grain (Pyr) associated with pore space. Sulfur content shown in yellow indicates sulfur retention in pore space. F) Creation of incipient porosity in association with pyrite. G) Isovolumetric weathering of rock via preservation of mineral grain shape. Kaolinite (Kaol) along fracture surface (right of picture) with Fe-oxide layer between the kaolinite and the rest of the rock. H) Dissolution of pyroxene (Pyx) in association with pyrite.

Fig. 3. Mineral composition (vol%) of parent rock minerals A) anorthite; B) albite; C) chlorite; D) pyroxene; E) epidote and F) quartz, determined via modal X-ray phase analysis. Each data point represents an average of 5 areas 2.8 × 2.1 mm of the same distance from the fracture surface. The hatched box represents the abundance in the parent rock ± 1SE. The dotted line indicates the visible rind. The grey shaded area is the uncertainty, presented as 1SE (n=5).

Fig. 4. Mineral composition (vol%) of secondary hydrothermal alteration minerals (top row) and secondary weathering product minerals (bottom row). A) apatite; B) sphene; C) pyrite; D) illite; E) Mn-oxides; F) Fe(III)-(hydr)oxides; G) kaolinite; H) gibbsite; determined via modal X-ray phase analysis. Each data point represents an average of 5 areas 2.8 × 2.1 mm of the same distance from the fracture surface. The hatched box represents the abundance in the parent rock ± 1SE. The dotted line indicates the visible rind. The grey shaded area is the uncertainty, presented as 1SE (n=5).

Fig. 5. A) Chemical index of alteration for the weathering profile (Eq. 1). B-D) Mass transfer (τ) profiles of elements in the weathering profile, calculated using Eq. 2, with Ti as the immobile element. The unfilled data points represent the ICP-OES data with the error bars representing 1SE of an internal standard, or where larger the detection limit of the method and propagated through all calculations. The filled data points represent the elemental X-ray data with the grey shaded area representing 1SE of the mean and propagated through all calculations. The vertical dotted line in each plot represents the tau value of the unweathered parent rock and the horizontal dotted line represents the visible rind. Note differing tau scales.

Fig. 6. A-D) Mass transfer (τ) profiles for more elements in the weathering profile; the unfilled data points represent the ICP-OES data with the error bars representing 1SE of an internal standard, or where larger the detection limit of the method and propagated through all calculations. The filled data points represent the elemental X-ray data with the grey shaded area representing 1SE of the mean and propagated through all calculations. E-F) Mass transfer (τ) profiles for U-series elements in the weathering profile. All mass transfer coefficients are calculated using Eq. 2, with Ti as the immobile. The vertical dotted line in each plot represents the tau value of the unweathered parent rock and the horizontal dotted line represents the visible rind. Note differing tau scales for each plot.

Fig. 7. Top x axis: Porosity (vol %) determined via modal X-ray phase analysis as a function of distance from the fracture surface. Bottom x axis: density ratio (unitless) calculated by dividing the density of unweathered rock by the density of weathered rock. Rock densities determined via mineral densities (Table 1) and mineral volumes (Fig. 3 and 4).

Fig. 8. Micro X-ray fluorescence map (µXRF) overlaying a BSE image, showing A) qualitative Fe(II) and Fe(III) content of a pyrite grain, the neighboring mineral (chlorite) and neighboring pore space (partially filled with kaolinite and gibbsite). Cream = Fe(II); Blue = Fe(III); and greyscale represents no Fe content. B) Qualitative S(VI) and S(-II) content of a pyrite grain and neighboring pore space (partially filled with kaolinite and gibbsite). White = S(-II); Red = S(VI) and greyscale represents no S content.

Fig. 9. Activity ratios of U-series nuclides A) ($^{234}U/^{238}U$) and B) ($^{230}Th/^{238}U$) in the weathering profile versus depth. The vertical dotted line represent secular equilibrium and the horizontal dotted line indicates the visible rind.

Fig. 10. Weathering gradients (bs) of normalized concentrations for A: albite; B: pyrite; C: epidote; D: chlorite; E: pyroxene in the B1W1 sample calculated using Eq. 4. With depletions relative to the parent material seen as decreases. All minerals show a linear trend for mineral dissolution.

Fig. 11. Comparison of the mineral dissolution rates (r_m) presented in this study (initial rate and rind rate) with those from the literature previously calculated for both lab and field. All lab rates are from Palandri and Kharaka (2004) and references therein. The field rates for each mineral are as follows: Epidote (Price et al., 2008); Albite (Buss et al., 2008); Chlorite (Buss et al., 2017); Pyroxene (Benedetti et al., 1994); Pyrite (Malmström et al., 2000).

Figure 1

Click here to download high resolution image

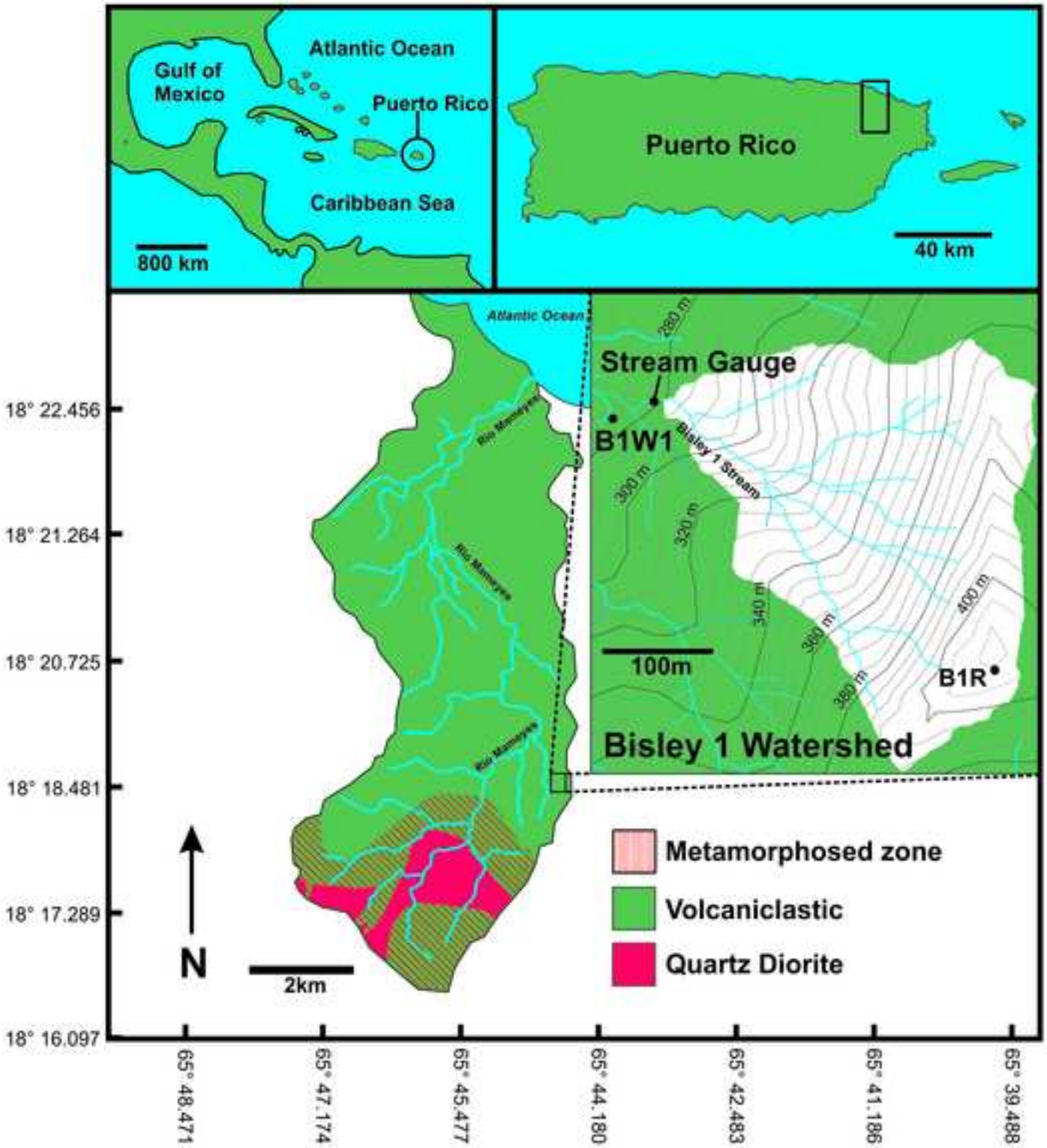

Figure 2

Click here to download high resolution image

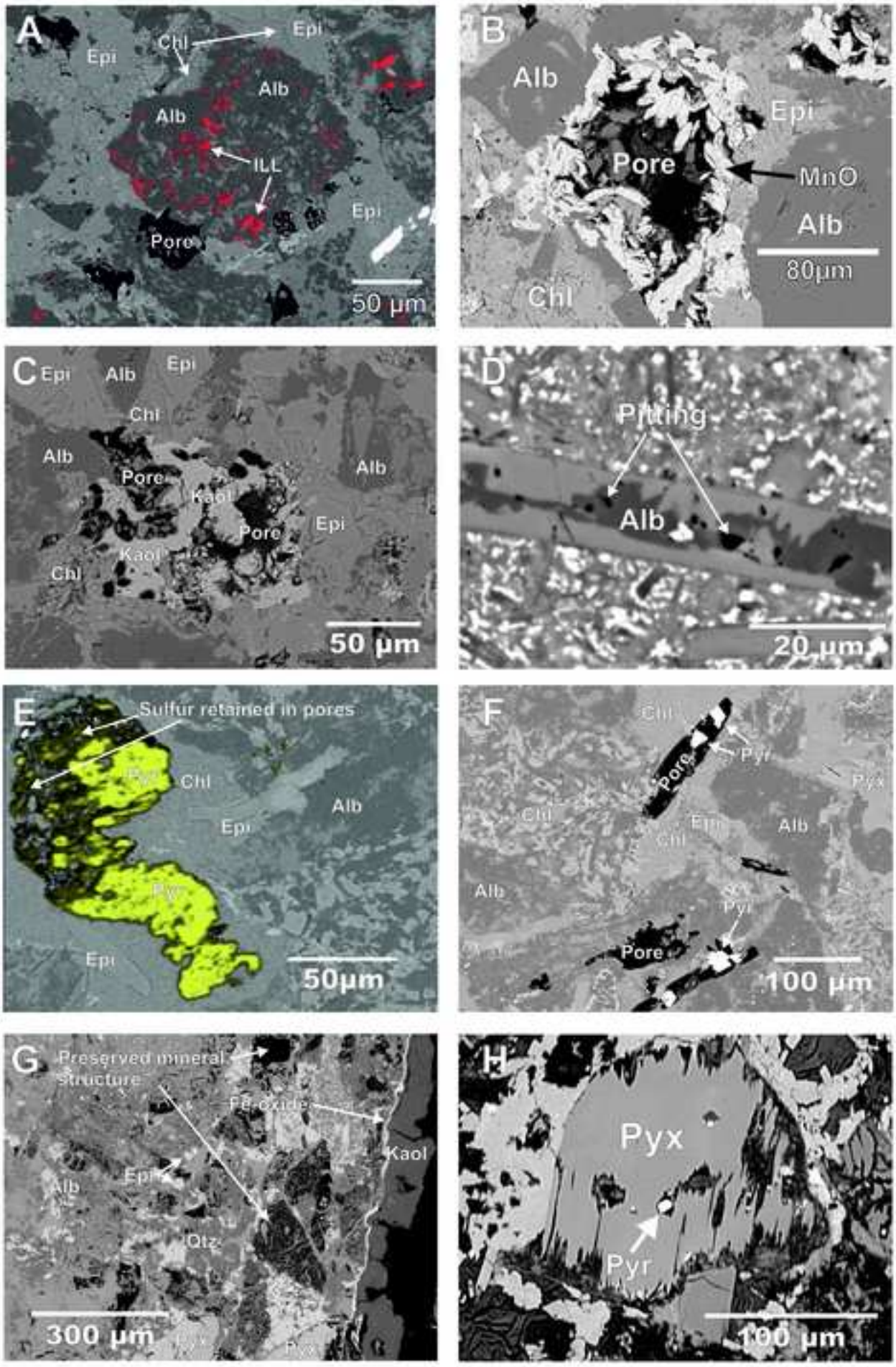

Figure 3

Click here to download high resolution image

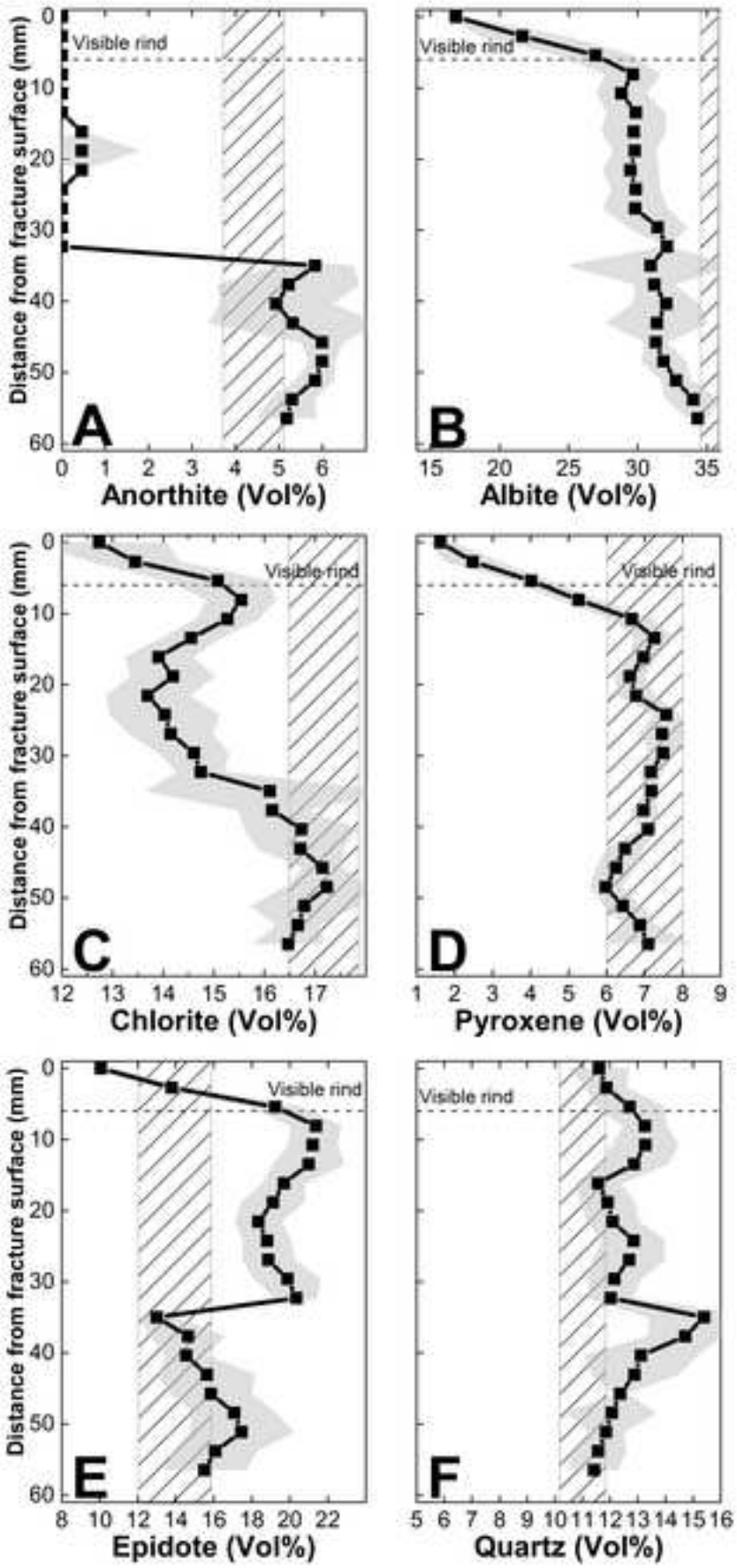

Figure 4

Click here to download high resolution image

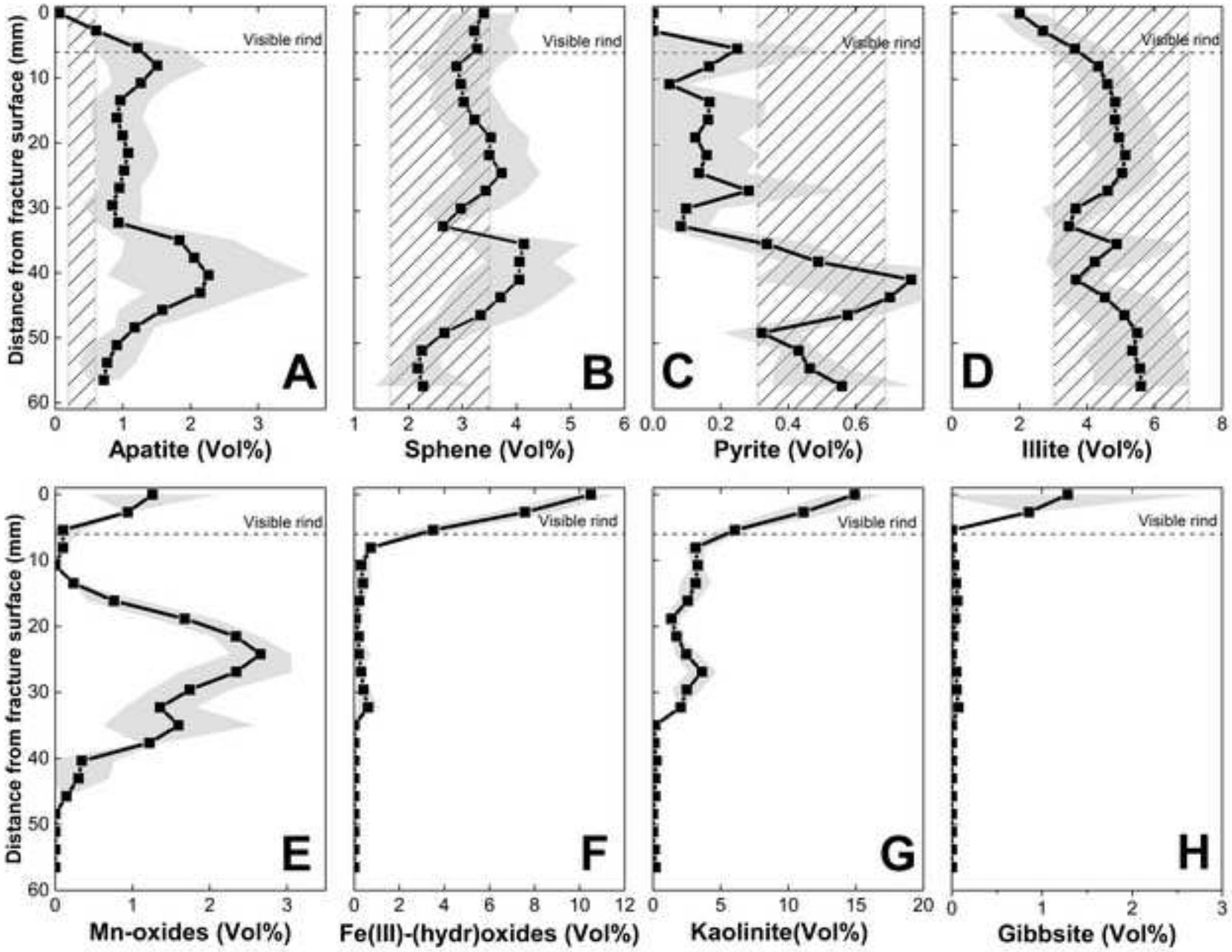

Figure 5

Click here to download high resolution image

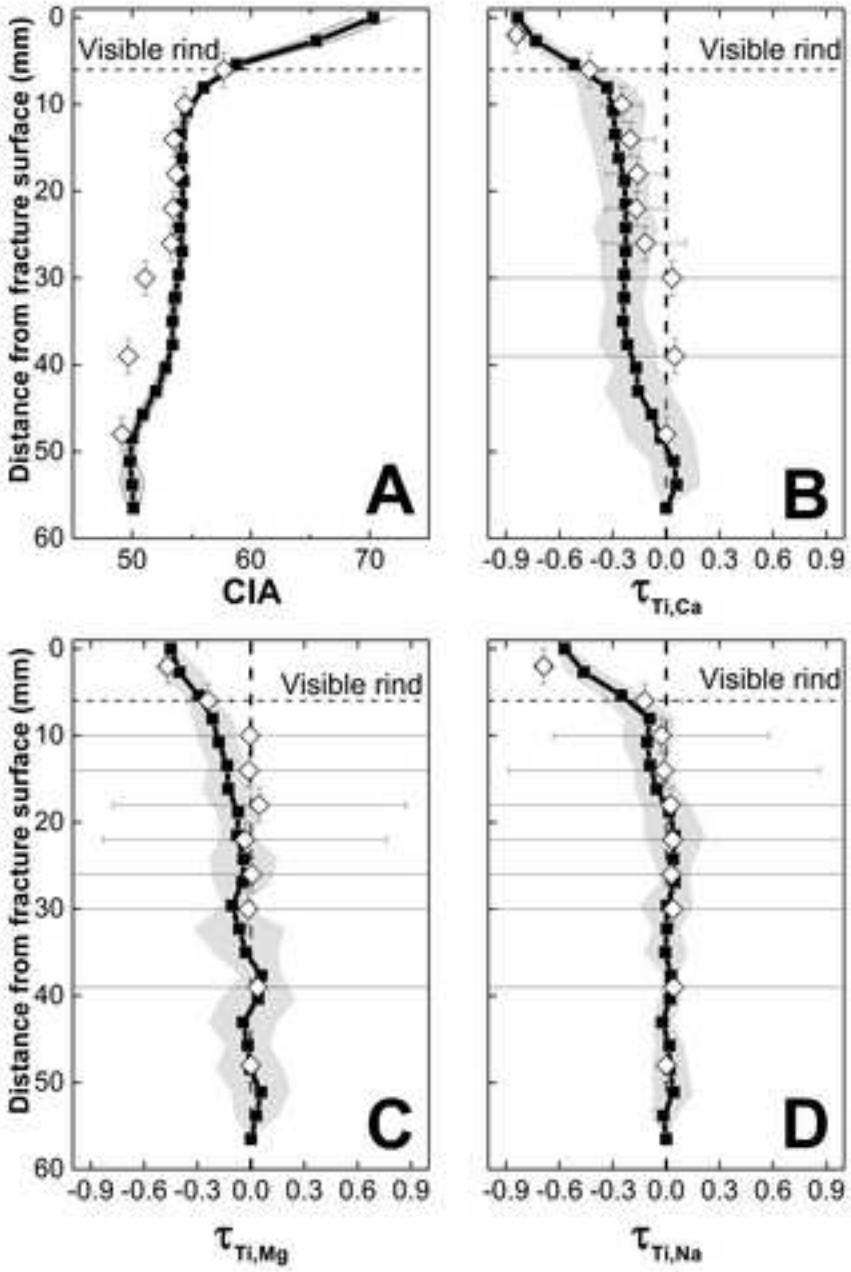

Figure 6

Click here to download high resolution image

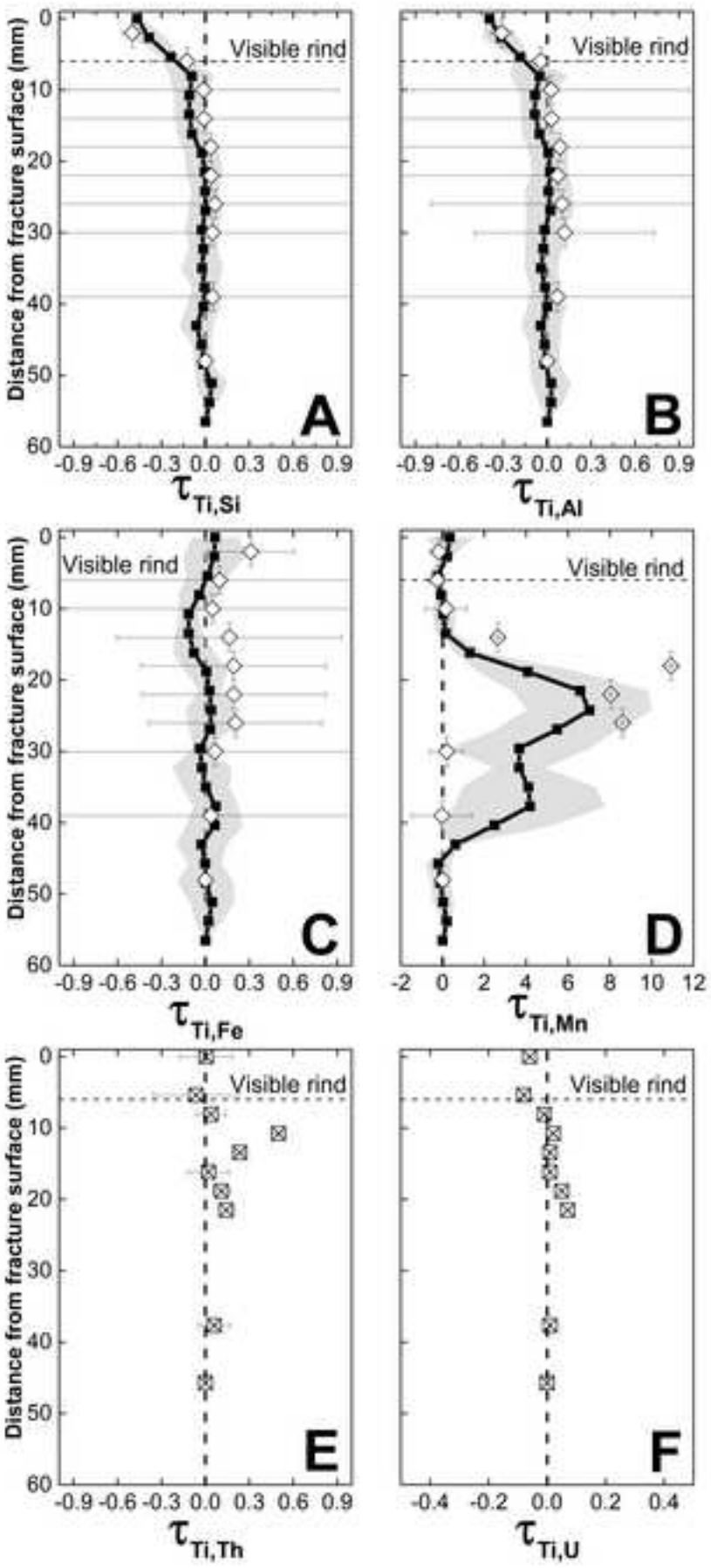

Figure 7

Click here to download high resolution image

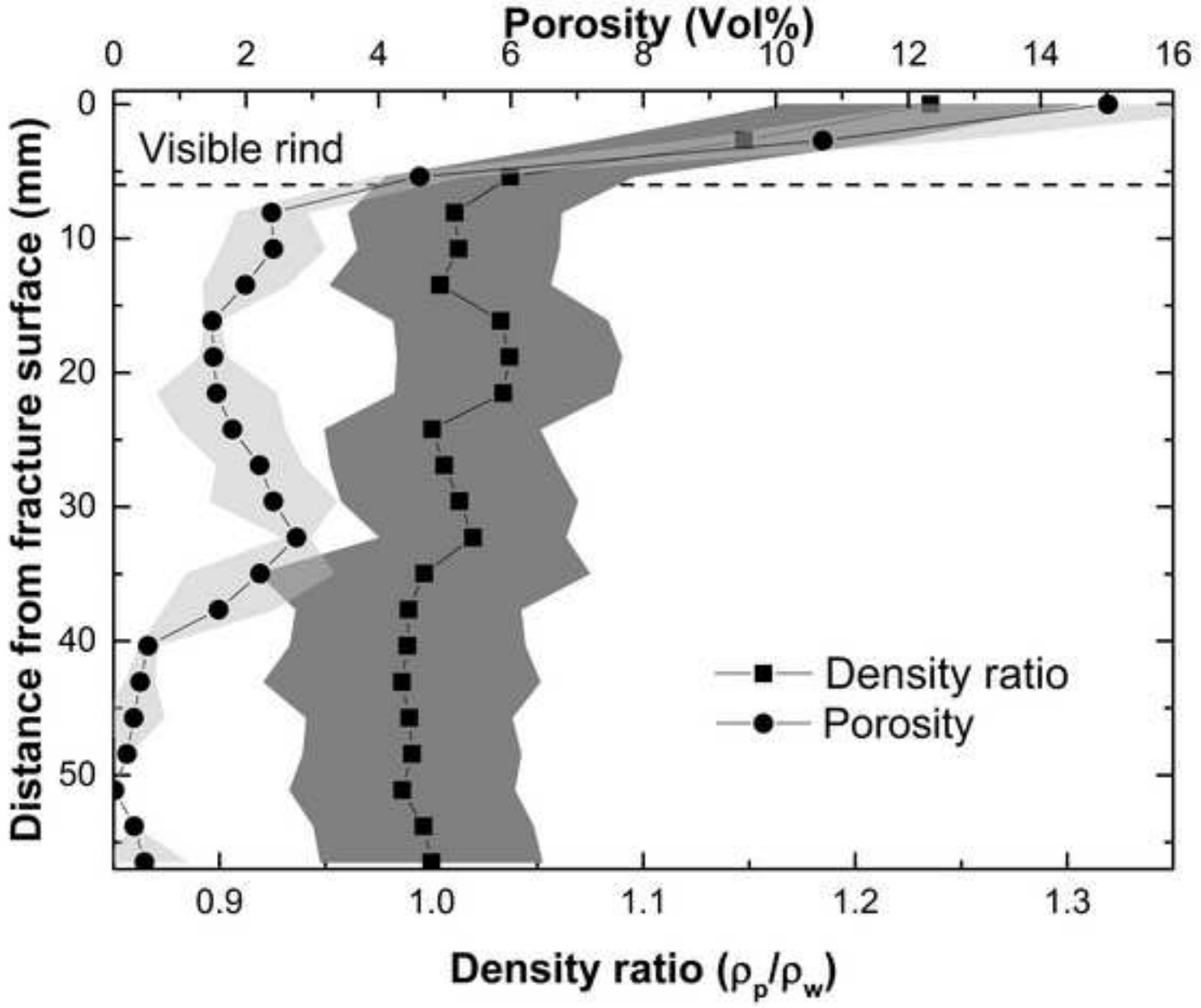

Figure 8

Click here to download high resolution image

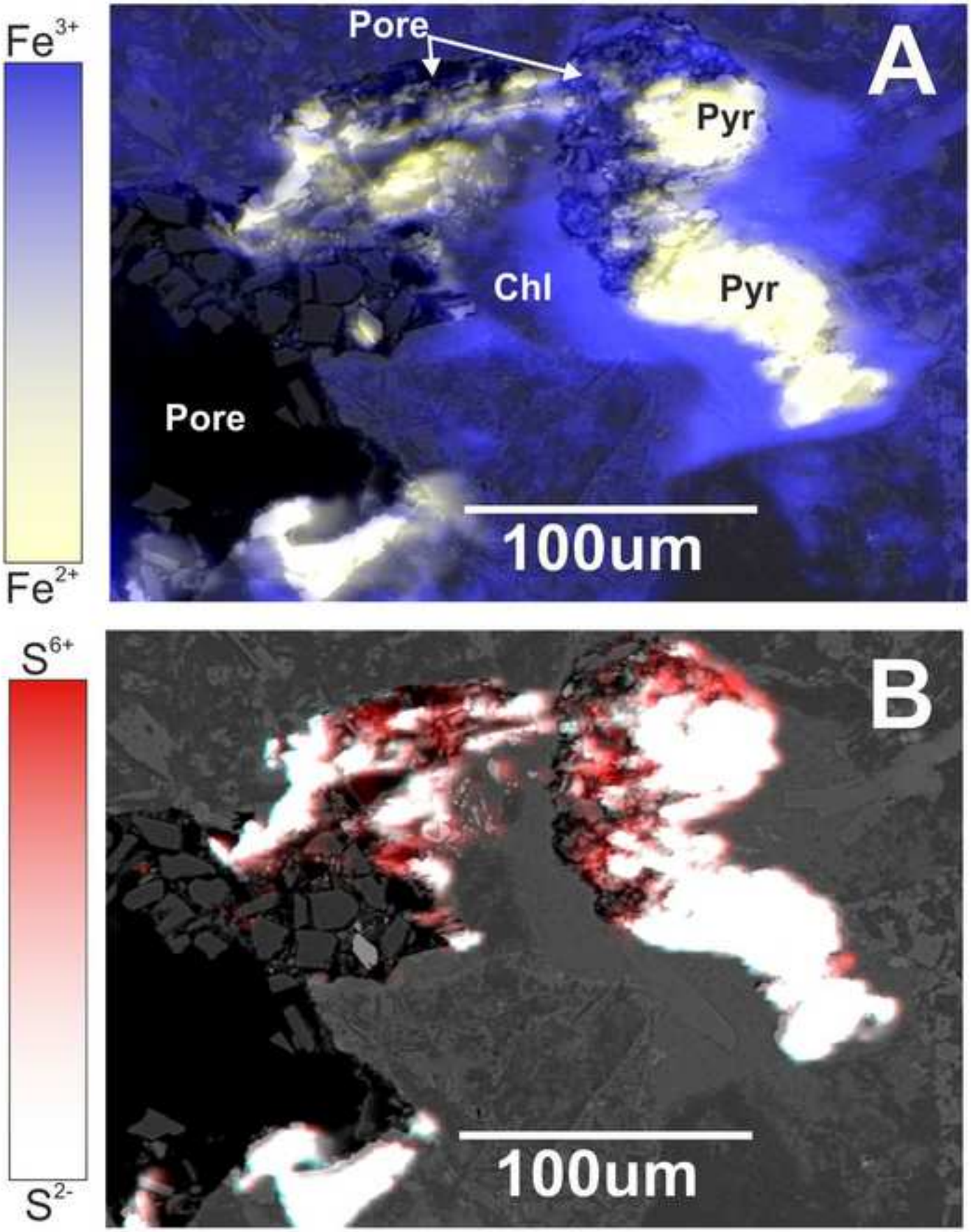

Figure 9

Click here to download high resolution image

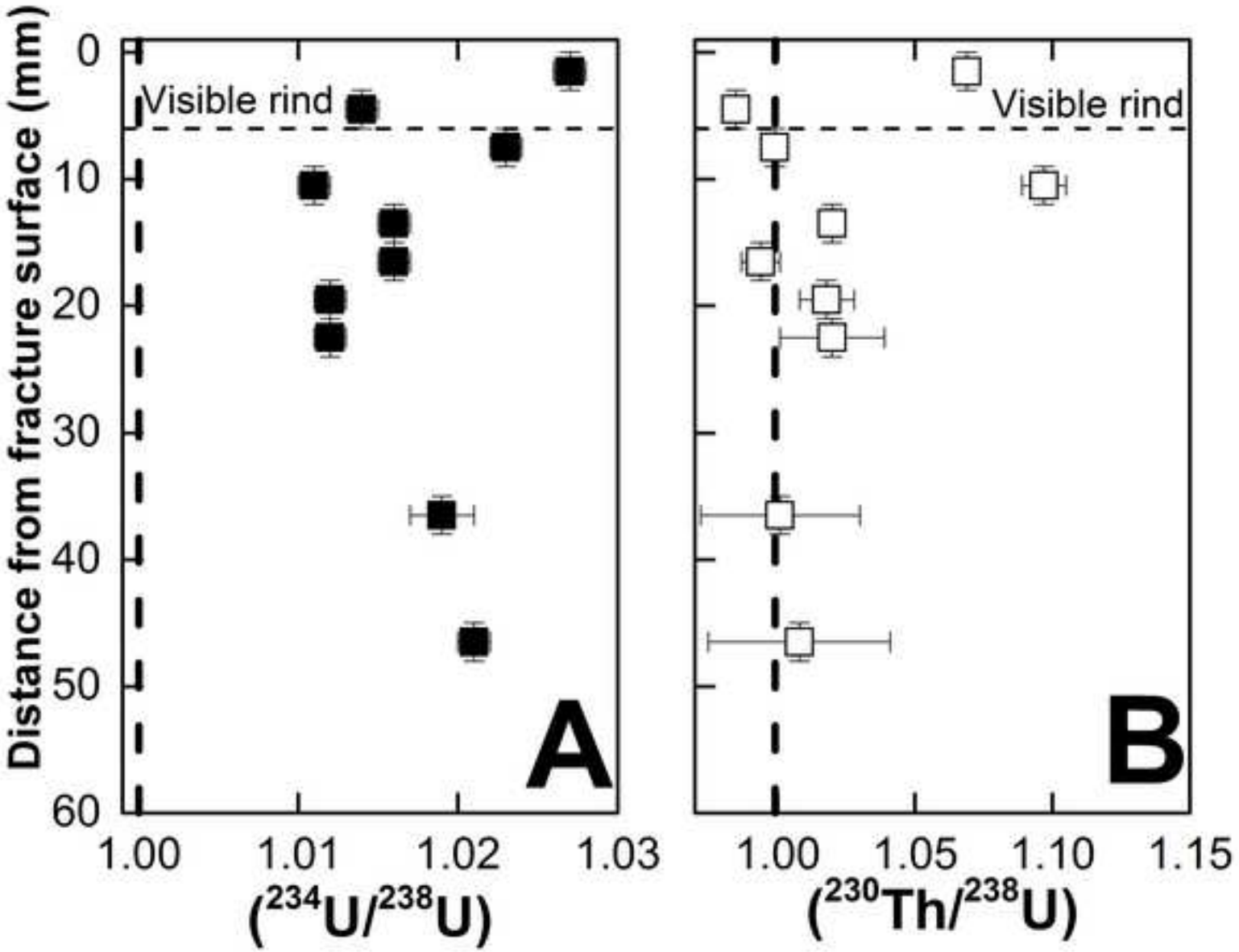

Figure 10

Click here to download high resolution image

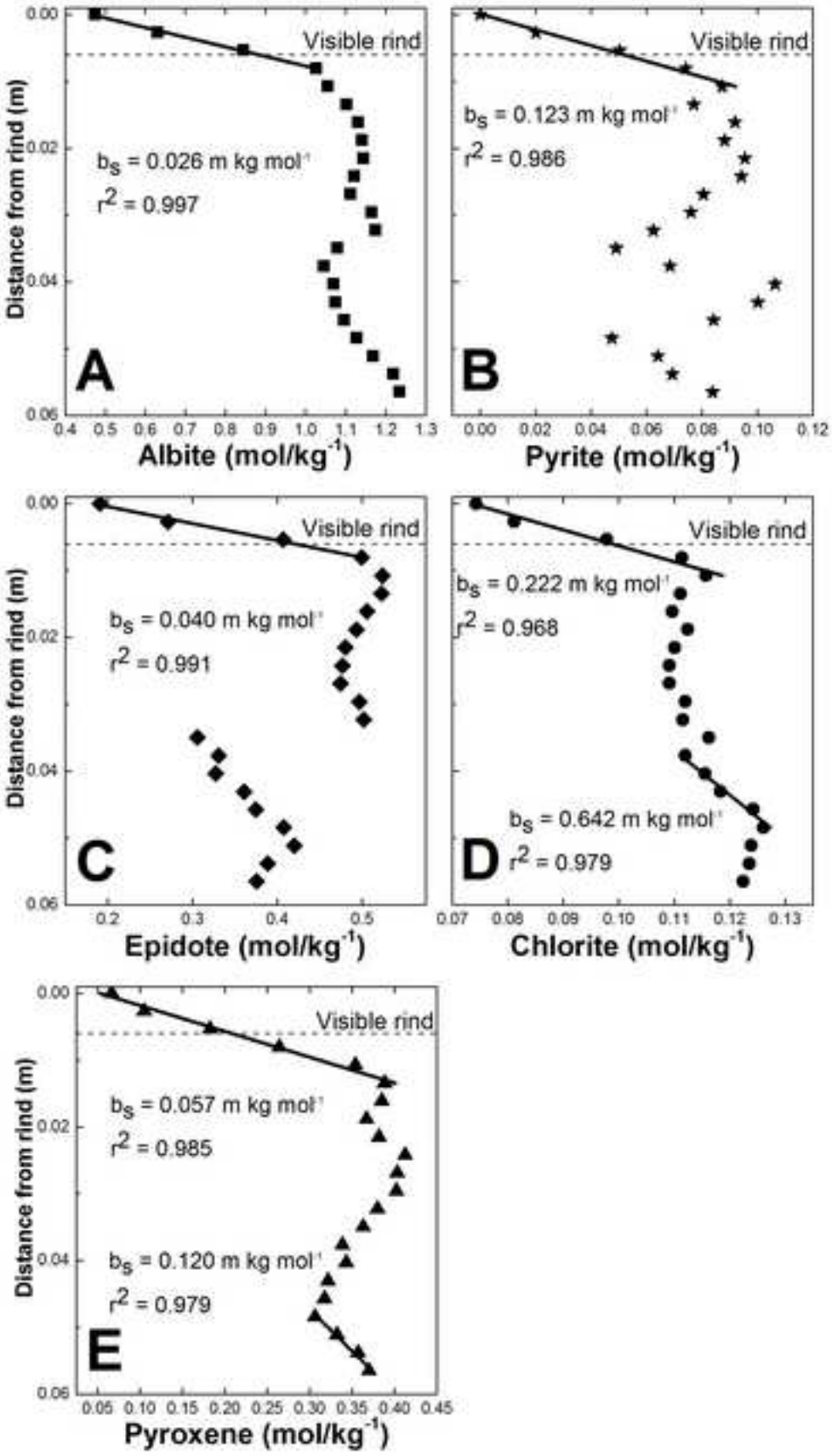

Figure 11

Click here to download high resolution image

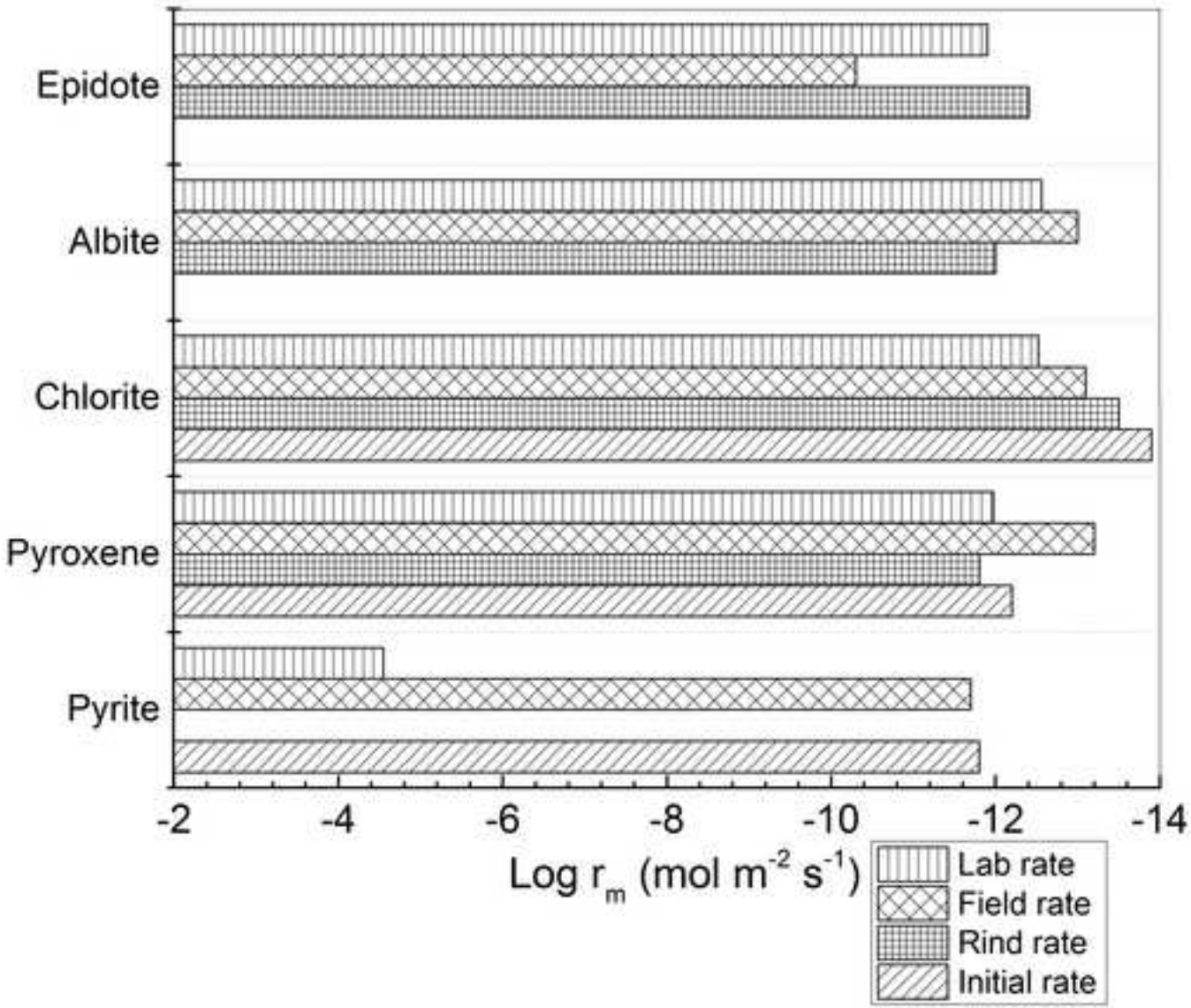

Supplementary Material

Click here to download Appendix: Moore 2018 GCA Supplementary R2.docx